



Defense Threat Reduction Agency
8725 John J. Kingman Road, MS
6201 Fort Belvoir, VA 22060-6201



DTRA-TR-15-36

TECHNICAL REPORT

Experimental & Numerical Investigation of Compact Dielectric Wakefield Accelerators

Distribution Statement A. Approved for public release; distribution is unlimited.

March 2016

HDTRA1-10-1-0051

Philippe Piot

Prepared by:
Northern Illinois Center for
Accelerator & Detector
Development
Northern Illinois University
DeKalb IL 60115

DESTRUCTION NOTICE:

Destroy this report when it is no longer needed.
Do not return to sender.

PLEASE NOTIFY THE DEFENSE THREAT REDUCTION
AGENCY, ATTN: DTRIAC/ J9STT, 8725 JOHN J. KINGMAN ROAD,
MS-6201, FT BELVOIR, VA 22060-6201, IF YOUR ADDRESS
IS INCORRECT, IF YOU WISH IT DELETED FROM THE
DISTRIBUTION LIST, OR IF THE ADDRESSEE IS NO
LONGER EMPLOYED BY YOUR ORGANIZATION.

REPORT DOCUMENTATION PAGE

*Form Approved
OMB No. 0704-0188*

Public reporting burden for this collection of information is estimated to average 1 hour per response, including the time for reviewing instructions, searching existing data sources, gathering and maintaining the data needed, and completing and reviewing this collection of information. Send comments regarding this burden estimate or any other aspect of this collection of information, including suggestions for reducing this burden to Department of Defense, Washington Headquarters Services, Directorate for Information Operations and Reports (0704-0188), 1215 Jefferson Davis Highway, Suite 1204, Arlington, VA 22202-4302. Respondents should be aware that notwithstanding any other provision of law, no person shall be subject to any penalty for failing to comply with a collection of information if it does not display a currently valid OMB control number. **PLEASE DO NOT RETURN YOUR FORM TO THE ABOVE ADDRESS.**

1. REPORT DATE (DD-MM-YYYY)			2. REPORT TYPE			3. DATES COVERED (From - To)	
4. TITLE AND SUBTITLE			5a. CONTRACT NUMBER				
			5b. GRANT NUMBER				
			5c. PROGRAM ELEMENT NUMBER				
6. AUTHOR(S)			5d. PROJECT NUMBER				
			5e. TASK NUMBER				
			5f. WORK UNIT NUMBER				
7. PERFORMING ORGANIZATION NAME(S) AND ADDRESS(ES)			8. PERFORMING ORGANIZATION REPORT NUMBER				
9. SPONSORING / MONITORING AGENCY NAME(S) AND ADDRESS(ES)			10. SPONSOR/MONITOR'S ACRONYM(S)				
			11. SPONSOR/MONITOR'S REPORT NUMBER(S)				
12. DISTRIBUTION / AVAILABILITY STATEMENT							
13. SUPPLEMENTARY NOTES							
14. ABSTRACT							
15. SUBJECT TERMS							
16. SECURITY CLASSIFICATION OF:			17. LIMITATION OF ABSTRACT	18. NUMBER OF PAGES	19a. NAME OF RESPONSIBLE PERSON		
a. REPORT	b. ABSTRACT	c. THIS PAGE			19b. TELEPHONE NUMBER (include area code)		

UNIT CONVERSION TABLE
U.S. customary units to and from international units of measurement*

U.S. Customary Units	Multiply by → ← Divide by [†]	International Units
Length/Area/Volume		
inch (in)	2.54 $\times 10^{-2}$	meter (m)
foot (ft)	3.048 $\times 10^{-1}$	meter (m)
yard (yd)	9.144 $\times 10^{-1}$	meter (m)
mile (mi, international)	1.609 344 $\times 10^3$	meter (m)
mile (nmi, nautical, U.S.)	1.852 $\times 10^3$	meter (m)
barn (b)	1 $\times 10^{-28}$	square meter (m^2)
gallon (gal, U.S. liquid)	3.785 412 $\times 10^{-3}$	cubic meter (m^3)
cubic foot (ft^3)	2.831 685 $\times 10^{-2}$	cubic meter (m^3)
Mass/Density		
pound (lb)	4.535 924 $\times 10^{-1}$	kilogram (kg)
unified atomic mass unit (amu)	1.660 539 $\times 10^{-27}$	kilogram (kg)
pound-mass per cubic foot ($lb\ ft^{-3}$)	1.601 846 $\times 10^1$	kilogram per cubic meter ($kg\ m^{-3}$)
pound-force (lbf avoirdupois)	4.448 222	newton (N)
Energy/Work/Power		
electron volt (eV)	1.602 177 $\times 10^{-19}$	joule (J)
erg	1 $\times 10^{-7}$	joule (J)
kiloton (kt) (TNT equivalent)	4.184 $\times 10^{12}$	joule (J)
British thermal unit (Btu) (thermochemical)	1.054 350 $\times 10^3$	joule (J)
foot-pound-force (ft lbf)	1.355 818	joule (J)
calorie (cal) (thermochemical)	4.184	joule (J)
Pressure		
atmosphere (atm)	1.013 250 $\times 10^5$	pascal (Pa)
pound force per square inch (psi)	6.984 757 $\times 10^3$	pascal (Pa)
Temperature		
degree Fahrenheit ($^{\circ}\text{F}$)	$[\text{T}({}^{\circ}\text{F}) - 32]/1.8$	degree Celsius (${}^{\circ}\text{C}$)
degree Fahrenheit ($^{\circ}\text{F}$)	$[\text{T}({}^{\circ}\text{F}) + 459.67]/1.8$	kelvin (K)
Radiation		
curie (Ci) [activity of radionuclides]	3.7 $\times 10^{10}$	per second (s^{-1}) [becquerel (Bq)]
roentgen (R) [air exposure]	2.579 760 $\times 10^{-4}$	coulomb per kilogram ($C\ kg^{-1}$)
rad [absorbed dose]	1 $\times 10^{-2}$	joule per kilogram ($J\ kg^{-1}$) [gray (Gy)]
rem [equivalent and effective dose]	1 $\times 10^{-2}$	joule per kilogram ($J\ kg^{-1}$) [sievert (Sv)]

* Specific details regarding the implementation of SI units may be viewed at <http://www.bipm.org/en/si/>.

[†]Multiply the U.S. customary unit by the factor to get the international unit. Divide the international unit by the factor to get the U.S. customary unit.

EXPERIMENTAL & NUMERICAL INVESTIGATION OF COMPACT DIELECTRIC WAKEFIELD ACCELERATORS (DWAs)

Philippe Piot^{1,2}, François Lemery¹, Ming-Chieh Lihm³,
Daniel Mihalcea¹, and Peter Stoltz³

¹ Northern Illinois Center for Accelerator & Detector Development
and Department of Physics, Northern Illinois University, DeKalb IL 60115, USA

² Accelerator Physics Center, Fermi National Accelerator Laboratory,
Batavia, IL 60510, USA

³ Tech-X Corporation, Boulder, CO 80303, USA

October 15, 2014

This final report summarized the work accomplished under the grant HDTRA-1-10-1-0051 to Northern Illinois University on R&D related to beam-driven dielectric accelerator – or dielectric-wakefield accelerator (DWA).

DISTRIBUTION STATEMENT A. Approved for public release; distribution is unlimited.

CONTENTS

1	Introduction	3
2	Development of efficient numerical simulation of wakefield acceleration	4
2.1	Wakefield generation	4
2.2	Dispersion equation & electromagnetic wakefields	6
2.2.1	Longitudinal Section Magnetic (LSM) modes	6
2.2.2	Longitudinal Section Electric (LSE) modes	7
2.2.3	Discussion	8
2.3	Wakefield amplitudes	8
2.4	Comparison with three-dimensional FDTD simulations	9
2.5	Two-dimensional limit	12
2.6	Implementation in a particle-in-cell beam dynamics program	13
3	Electron-bunch shaping for enhanced transformer ratio	18
3.1	Tradeoffs between transformer ratio and peak accelerating field	18
3.1.1	Simulation Methods	18
3.1.2	Results	19
3.2	Optimum electron-bunch shape	21
3.2.1	Smooth current profiles for enhanced transformer ratios	22
3.2.2	Beam shaping using a tailored photocathode laser	24
3.3	Experimental realization of a linearly-ramped bunch with a multifrequency linac	27
4	Experimental setup for slab-dielectric structure test at Fermilab	31
4.1	experimental setup	31
4.2	Start-to-end simulations	33
4.2.1	Case of single-mode DLW structures	33
4.2.2	Case of multi-mode DLW structures	34
4.3	Conclusion & Outlook	36
5	Bench test of a dielectric structure	37
5.1	Experimental Setup	37
5.2	Simulation and Analysis of a THz pulse propagation in a SLAB DLW	38
5.3	Status and Conclusion	40
6	Education & Collaboration	40
7	Publications, and presentation	41
7.1	Talks	41
7.2	Referred Publications:	42
7.3	Conference proceedings papers:	42

1 INTRODUCTION

Electron accelerators capable of producing high-quality electron beam with energies of 10-20 Mega-electron-Volt (MeV) are finding an increasing number of applications in our Society. Such applications include medicine (oncology, and imaging), industry (e.g. lithography), security, and discovery sciences. On another hand, over the last two decade, needs in elementary particle physics have driven the development of new acceleration techniques capable of producing very high accelerating field [Giga-electron-Volt per meter (GV/m) electric fields]. These techniques could in turn be transplanted to low and medium energy accelerator thereby resulting in tabletop easy-to-operate devices that could proliferate to small-scale laboratories in industrial settings, hospital and Universities. Beside enabling a wide range of research this table-top accelerator could support the accelerator-based light source capable of producing X rays.

The main goal of the proposed research was to explore the use of wakefield accelerators – a concept developed in support to high-energy particle accelerator – as path toward the realization of compact accelerator with 10-20 MeV output energy.

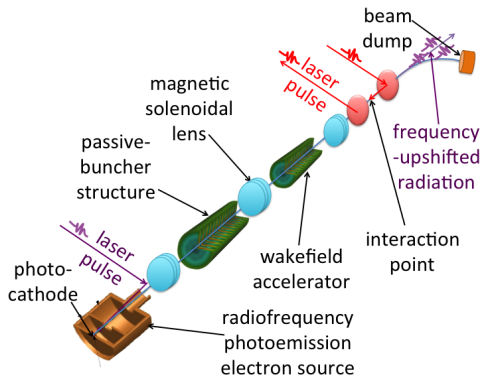


Figure 1: Schematic rendition of the wakefield driven X-ray source concept. In this version of the concept both passive bunch and wakefield-accelerator structures are dielectric-lined waveguides (DLW's). The red cylindrical objects are injection and ejection mirrors for the laser.

Our approach toward the development of a compact beam-driven accelerator consists of four main components depicted in Fig. 1. The production of a bunch suitable for beam-driven acceleration is enable by the combination of a conventional L-band radiofrequency (RF) photoemission source coupled to a “passive buncher”. In this approach a sub-5 MeV electron bunch emitted from the RF gun is transversely focused into a high-impedance structure (e.g. a dielectric-lined waveguide, or a corrugated structure). The self-interaction of the bunch with its short-range wakefield imparts longitudinal-phase-space correlations suitable for attaining high peak current as the bunch drift in a free space. The structure geometry and electron-beam parameters are optimized to form a high-peak-current “drive” bunch followed by a lower charge “witness” bunch . The two-bunch system is then sent

to a dielectric-lined waveguide (DLW) with parameters optimized so that the wakefield produced by the drive bunch accelerates the witness bunch. In a last stage, after disposal of the drive bunch, the witness electron bunch is collided head-on with a ultrafast laser thereby producing radiation with upshifted frequency $\omega \sim 4\gamma^2\omega_L$ where γ is the witness bunch Lorentz' factor and $\omega_L = 2\pi c/\lambda_L$ with λ_L being the laser wavelength.

2 DEVELOPMENT OF EFFICIENT NUMERICAL SIMULATION OF WAKEFIELD ACCELERATION

2.1 WAKEFIELD GENERATION

The geometry of the problem analyzed in this paper is depicted in Fig. 2. Transient effects resulting from the injection of the electron bunch in the structure are not included (the structure is assumed to be infinitely long) and the drive bunch is taken to be ultra-relativistic with its Lorentz factor γ much greater than unity. The longitudinal motion of the drive bunch is assumed to be at a constant speed v and the origin of the z -axis is chosen such that $z = vt$ where t is the time. The bunch is modelled has a superimposition of line of charges with finite extension in horizontal direction and with an offset y_0 in the vertical direction.

$$\rho(x, y, z) = \sum_m \lambda_m \cos(k_{x,m}x) \delta(y - y_0) \delta(z - vt), \quad (1)$$

The line-charge distribution is taken to be symmetric with respect to the vertical y -axis [$\rho(x, y, z) = \rho(-x, y, z)$] and vanishes at the dielectric and metallic boundary surfaces [$\rho(-L_x/2, y, z) = \rho(L_x/2, y, z) = \rho(x, a, z) = \rho(x, -a, z) = 0$]. Under these assumptions the charge distribution can be written as a Fourier series in the horizontal direction

$$\rho(x, y, z) = \sum_m \lambda_m \cos(k_{x,m}x) \delta(y - y_0) \delta(z - vt), \quad (2)$$

where λ_m is a constant and each term is indexed by the integer $m = 0, 1, \dots$ defined such that $k_x \equiv (2m+1)\frac{\pi}{L_x}$. In the vacuum region and away outside the charge distribution the wakefield satisfies the wave equation:

$$\left(\nabla^2 - \frac{1}{c^2} \frac{\partial^2}{\partial^2 t} \right) \mathbf{E} = 0. \quad (3)$$

In this paper we consider only the propagating modes with harmonic longitudinal and temporal dependencies of the form $\mathbf{E}(x, y, z, t) = \mathbf{E}(x, y)e^{i(\omega t - k_z z)}$ where $k_z = \mathbf{k} \cdot \hat{\mathbf{z}}$. In addition to the propagating-mode solutions, Eq. 3 when subject to the boundary conditions also admits evanescent modes with imaginary eigen-frequencies ω . Since these evanescent modes are present over short distances behind the drive bunch, they do not contribute to the beam dynamics of a subsequent witness bunch. These short-range fields are consequently ignored in the remaining of this paper.

In the ultra-relativistic regime and considering the modes to be synchronous with the beam by imposing their phase velocity to satisfy $v_\varphi \equiv \frac{\omega}{k_z} = v \approx c$. The transverse

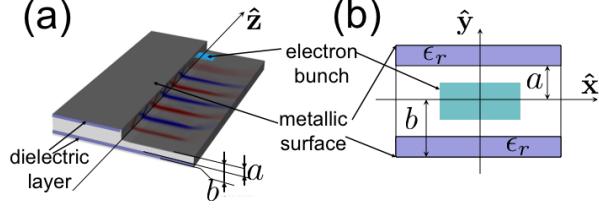


Figure 2: Overview of the DLW structure geometry (left) and transverse cross section (right). A rectangular-shaped drive beam is displayed in blue.

wavevector $k_{\perp} \equiv \sqrt{k^2 - k_z^2} \simeq k/\gamma = 0$ the wave equation 3 can be written only in terms of the partial derivatives with respect to the transverse coordinates

$$\nabla_{\perp}^2 \mathbf{E}(x, y) = 0. \quad (4)$$

The symmetry of drive-beam charge distribution and the boundary conditions at $x = \pm L_x/2$, determine (up to constants) the analytical expression of the fields. In the vacuum region. The electric field components are simple combinations of trigonometric and hyperbolic functions:

$$\begin{aligned} E_x &\propto \sin(k_{x,m}x) \cosh(k_y y), \\ E_y &\propto \cos(k_{x,m}x) \sinh(k_y y), \\ E_z &\propto \cos(k_{x,m}x) \cosh(k_y y). \end{aligned} \quad (5)$$

The axial field E_z associated with this set of solution is symmetric with respect to the horizontal axis [i.e. $E_z(x, -y, z) = E_z(x, y, z)$] we henceforth refer this set to as "monopole" modes. Similarly, a set of field with an antisymmetric axial field [$E_z(x, -y, z) = -E_z(x, y, z)$] is obtained by substitution of $\sinh(k_y y)$ with $\cosh(k_y y)$ and vice versa. This latter set is termed as "dipole" modes in the remaining of this paper.

Inside the dielectric, the transverse wave number cannot be neglected

$$k_{\perp}^2 \equiv k_{x,m}^2 + k_y^2 \approx \frac{\omega^2}{c^2} (\epsilon_r - 1) > 0, \quad (6)$$

where ϵ_r is the relative electric permittivity of the dielectric medium. The boundary conditions at $y = \pm b$ and at $x = \pm L_x/2$ determine the trigonometric form of the field expressions. Inside the dielectric region, there is no distinction between monopole and dipole modes and the electric field components are given by

$$\begin{aligned} E_x &\propto \sin(k_{x,m}x) \cos[k_y(b - y)], \\ E_y &\propto \cos(k_{x,m}x) \sin[k_y(b - y)], \\ E_z &\propto \cos(k_{x,m}x) \cos[k_y(b - y)]. \end{aligned} \quad (7)$$

The corresponding expressions for the magnetic field in the vacuum and dielectric regions can be easily obtained following a similar prescription.

Inspection of the z -component of the fields indicates that the normal modes cannot be categorized in the usual transverse electric or transverse magnetic sets. The reason is that the separation surface between the dielectric and vacuum regions is in the $x - z$ plane unlike the case of the uniformly-filled waveguides where this surface is in the transverse $x - y$ plane.

Therefore, it is natural to categorize the modes depending on the orientation of the fields with respect to the dielectric surface. Following the definition introduced in Ref. we classify the mode as Longitudinal Section Magnetic (LSM) and Longitudinal Section Electric (LSE) modes corresponding respectively to the case when the magnetic and electric field component perpendicular to the dielectric surface is vanishes. In the configuration shown in Fig. 2, LSE and LSM modes correspond respectively to $E_y = 0$ and $H_y = 0$ at the vacuum-dielectric interface.

2.2 DISPERSION EQUATION & ELECTROMAGNETIC WAKEFIELDS

2.2.1 LONGITUDINAL SECTION MAGNETIC (LSM) MODES

To obtain the normal mode frequencies it is convenient to use the hertzian potential vector method . In the source-free region, magnetic and electric fields can be expressed in terms of the vector potential $\boldsymbol{\Pi}$:

$$\mathbf{H} = i\omega\epsilon\nabla \times \boldsymbol{\Pi}, \quad (8)$$

$$\mathbf{E} = k^2\boldsymbol{\Pi} + \nabla(\nabla \cdot \boldsymbol{\Pi}), \quad (9)$$

where $\boldsymbol{\Pi}$ is the solution of the homogeneous Helmholtz equation in the vacuum region. To determine the frequencies and the fields for the modes when $H_y = 0$ (LSM) it is convenient to choose $\boldsymbol{\Pi} \equiv \boldsymbol{\Pi}_e = \psi_e(x, y)e^{i(\omega t - k_z z)}\hat{\mathbf{y}}$ where the scalar function $\psi_e(x, y)$ must be a solution of $(\nabla_{\perp}^2 + k_{\perp}^2)\psi_e = 0$. From Eqs. 8 and 9 all fields can be expressed in terms of the unknown function $\psi_e(x, y)$:

$$\begin{aligned} E_x &= \frac{\partial^2 \psi_e}{\partial x \partial y} & H_x &= -\epsilon k_z^2 c \psi_e \\ E_y &= k^2 \psi_e + \frac{\partial^2 \psi_e}{\partial y^2} & H_y &= 0 \\ E_z &= -ik_z \frac{\partial \psi_e}{\partial y} & H_z &= i\epsilon k_z c \frac{\partial \psi_e}{\partial x} \end{aligned} \quad (10)$$

The expression for ψ_e that satisfies Eqns. 10, 6, and 8 is given by:

$$\psi_e = \begin{cases} A \cos(k_{x,m}x) \sinh(k_{x,m}y), & 0 < y < a \\ B \cos(k_{x,m}x) \cos[k_y(b-y)], & a < y < b \end{cases} \quad (11)$$

where A and B are constants. The boundary conditions completely determine the eigen-frequencies of the LSM modes. Since H_x ($\propto \epsilon \psi_e$) and E_z ($\propto \frac{\partial \psi_e}{\partial y}$) are continuous at $y = a$ the constants A and B can be eliminated giving the dispersion equation

$$\coth(k_{x,m}a) \cot[k_y(b-a)] = \frac{k_y}{\epsilon_r k_{x,m}}. \quad (12)$$

Therefore each discrete value of $k_{x,m}$ there is an infinite set of discrete $k_{y,n}$ values where n is an integer. So, the eigenfrequencies are indexed by the integer couple (m, n) and verify

$$k_{x,m}^2 + k_{y,n}^2 = \frac{\omega_{m,n}^2}{c^2}(\epsilon_r - 1). \quad (13)$$

It worthwhile noting that the boundary conditions do not completely determine either the function ψ_e or the fields. The reason being that, up to this point, the field source terms (ρ, \mathbf{j}) were not taken into account although their symmetries were invoked. Still, it is straightforward to show that all fields associated to one set of mode (and also ψ_e) depend have a common normalization constant, the amplitude $E_{0;m,n}$, which remains to be determined. The expressions of the fields are given by

$$\begin{aligned} E_{x,m,n} &= \begin{cases} -\frac{iE_{0;m,n}k_{x,m}}{k_z} \sin(k_{x,m}x) \cosh(k_{x,m}y) & 0 < y < a \\ -\frac{iE_{0;m,n}k_{x,m}}{k_z} \frac{\cosh(k_{x,m}a)}{\sin[k_{y,n}(b-a)]} \sin(k_{x,m}x) \sin[k_{y,n}(b-y)] & a < y < b \end{cases} \\ E_{y,m,n} &= \begin{cases} \frac{iE_{0;m,n}}{k_{x,m}k_z} (k_{x,m}^2 + k_z^2) \cos(k_{x,m}x) \sinh(k_{x,m}y) & 0 < y < a \\ \frac{iE_{0;m,n} \cosh(k_{x,m}a)}{k_{y,n}k_z \sin[k_{y,n}(b-a)]} (k_z^2 + k_{x,m}^2) \cos(k_{x,m}x) \cos[k_{y,n}(b-y)] & a < y < b \end{cases} \\ E_{z,m,n} &= \begin{cases} E_{0;m,n} \cos(k_{x,m}x) \cosh(k_{x,m}y) & 0 < y < a \\ E_{0;m,n} \frac{\cosh(k_{x,m}a)}{\sin[k_{y,n}(b-a)]} \cos(k_{x,m}x) \sin[k_{y,n}(b-y)] & a < y < b \end{cases} \\ H_{x,m,n} &= \begin{cases} \frac{iE_{0;m,n}k_z\epsilon c}{k_{x,m}} \cos(k_{x,m}x) \sinh(k_{x,m}y) & 0 < y < a \\ -\frac{iE_{0;m,n}k_z\epsilon c}{k_{x,m}} \frac{\cosh(k_{x,m}a)}{\sin[k_{y,n}(b-a)]} \cos(k_{x,m}x) \cos[k_{y,n}(b-y)] & a < y < b \end{cases} \\ H_{y,m,n} &= 0 \\ H_{z,m,n} &= \begin{cases} E_{0;m,n}\epsilon c \sin(k_{x,m}x) \sinh(k_{x,m}y) & 0 < y < a \\ \frac{E_{0;m,n}k_{x,m}\epsilon c}{k_{y,n}} \frac{\cosh(k_{x,m}a)}{\sin[k_{y,n}(b-a)]} \sin(k_{x,m}x) \cos[k_{y,n}(b-y)] & a < y < b \end{cases} \end{aligned} \quad (14)$$

2.2.2 LONGITUDINAL SECTION ELECTRIC (LSE) MODES

The case of the LSE modes ($E_y = 0$) can be treated in a similar fashion than for the LSM modes. The hertzian vector electric potential is replaced by a vector magnetic potential $\mathbf{\Pi}_h$ which is related to the fields:

$$\mathbf{E} = -i\omega\mu\nabla \times \mathbf{\Pi}_h \quad (15)$$

$$\mathbf{H} = k^2 \mathbf{\Pi}_h + \nabla(\nabla \cdot \mathbf{\Pi}_h) \quad (16)$$

As in the previous case, it is convenient to factor out the t and z -dependencies of the $\mathbf{\Pi}_h$ and to define a scalar function $\psi_h(x, y)$: $\mathbf{\Pi}_h = \psi_h(x, y)e^{i(\omega t - k_z z)}\hat{\mathbf{y}}$. It is straightforward to derive the dispersion equation for the LSE modes

$$\coth(k_x a) \cot[k_y(b - a)] = -\frac{k_x}{k_y}, \quad (17)$$

and the expressions for the electromagnetic-field components:

$$\begin{aligned} E_{x,m,n} &= \begin{cases} -\frac{iE_{0;m,n}k_z}{k_{x,m}} \sin(k_{x,m}x) \cosh(k_{x,m}y) & 0 < y < a \\ -\frac{iE_{0;m,n}k_z}{k_{x,m}} \frac{\cosh(k_{x,m}a)}{\sin[k_{y,n}(b-a)]} \sin(k_{x,m}x) \sin[k_{y,n}(b-y)] & a < y < b \end{cases} \\ E_{y,m,n} &= 0 \\ E_{z,m,n} &= \begin{cases} E_{0;m,n} \cos(k_{x,m}x) \cosh(k_{x,m}y) & 0 < y < a \\ E_{0;m,n} \frac{\cosh(k_{x,m}a)}{\sin[k_{y,n}(b-a)]} \cos(k_{x,m}x) \sin[k_{y,n}(b-y)] & a < y < b \end{cases} \\ H_{x,m,n} &= \begin{cases} \frac{iE_{0;m,n}k_{x,m}}{k_z \mu c} \cos(k_{x,m}x) \sinh(k_{x,m}y) & 0 < y < a \\ -\frac{iE_{0;m,n}k_{y,n}}{k_z \mu c} \frac{\cosh(k_{x,m}a)}{\sin[k_{y,n}(b-a)]} \cos(k_{x,m}x) \cos[k_{y,n}(b-y)] & a < y < b \end{cases} \\ H_{y,m,n} &= \begin{cases} \frac{iE_{0;m,n}(k_{x,m}^2 + k_z^2)}{k_{x,m}k_z \mu c} \sin(k_{x,m}x) \cosh(k_{x,m}y) & 0 < y < a \\ \frac{iE_{0;m,n}(k_{x,m}^2 + k_z^2)}{k_{x,m}k_z \mu c} \frac{\cosh(k_{x,m}a)}{\sin[k_{y,n}(b-a)]} \sin(k_{x,m}x) \cos[k_{y,n}(b-y)] & a < y < b \end{cases} \\ H_{z,m,n} &= \begin{cases} \frac{E_{0;m,n}}{\mu c} \sin(k_{x,m}x) \sinh(k_{x,m}y) & 0 < y < a \\ -\frac{E_{0;m,n}k_y}{k_{x,m}\mu c} \frac{\cosh(k_{x,m}a)}{\sin[k_{y,n}(b-a)]} \sin(k_{x,m}x) \cos[k_{y,n}(b-y)] & a < y < b \end{cases} \end{aligned} \quad (18)$$

2.2.3 DISCUSSION

For higher-order modes the solutions of both LSM and LSE dispersion equations tend to be equally spaced. For large values of $x \equiv k_y(b - a)$, the solutions of the transcendental equations 12 and 17 approach $p\pi$ and $(p + \frac{1}{2})\pi$ respectively where the $p \gg 1$ is an integer.

The dispersion equations for the LSM and LSE dipole modes is obtained by substituting $\tanh(k_{x,m}a)$ for $\coth(k_{x,m}a)$ in Equations. 12 and 17 respectively.

An important property of the wakefields described by Eqns. 14 and 18 is that the phase difference between the longitudinal and transverse components is always $\pm\frac{\pi}{2}$ no matter what the mode type is. This means that whenever the longitudinal force, $F_z = qE_z$, reaches a minimum (drive bunch) or a maximum (test bunch), the vertical force, $F_y = q(E_y + vB_x)$ is zero. The important consequence is that the beam breakup cannot happen for these kind of structures provided the electron bunch length is much shorter than the wavelength of the fundamental mode.

2.3 WAKEFIELD AMPLITUDES

Although we have obtained the general expression for the electromagnetic field, the constant $E_{0;m,n}$ still remained to be determined. An often used method to find the constant

$E_{0;m,n}$ in Eqns. 14 and 18, is to evaluate the Green function of the wave equation with sources included. The latter is usually a cumbersome procedure and we instead chose to determine $E_{0;m,n}$ based on energy balance considerations. The electromagnetic energy stored in the DLW equals the mechanical work performed on the drive bunch. The key point here is to invoke the fundamental wakefield theorem . For a linear wakefield, the decelerating field E_d acting on a drive point-charge is half of the wakefield amplitude, i.e. $E_d = \frac{E_{0;m,n}}{2}$. Suppose the drive charge moves over an infinitely short distance δz . The work performed by the wakefield on the drive charge should equate the energy stored in the field

$$\begin{aligned} & \sum_{m,n} \int \delta(y - y_0) \frac{E_{z;m,n}(z = vt)}{2} dx dy \delta z \\ &= \frac{1}{2} \int (\epsilon E^2 + \mu_0 H^2) dx dy \delta z, \end{aligned} \quad (19)$$

where the integration extends over the transverse plane. It is straightforward to evaluate the full expressions of the wakefield amplitudes in terms of the wave numbers $k_{x,m}$ and $k_{y,n}$ from Eqns. 19, 14 and 18:

$$\begin{aligned} E_{0;m,n}^{LSM} &= \frac{1}{2\epsilon_0} \frac{\lambda_m \cosh(k_{x,m} y_0)}{\frac{\sinh(2k_{x,m}a)}{2k_{x,m}} + \frac{\epsilon_r \cosh^2(k_{x,m}a)}{\sin^2[k_{y,n}(b-a)]} \left\{ \frac{b-a}{2} \left(1 + \frac{\epsilon_r k_{x,m}^2}{k_{y,n}^2} \right) - \frac{\sin[2k_{y,n}(b-a)]}{4k_{y,n}} \left(1 - \frac{\epsilon_r k_{x,m}^2}{k_{y,n}^2} \right) \right\}} \\ E_{0;m,n}^{LSE} &= \frac{1}{2\epsilon_0} \frac{\lambda_m \cosh(k_{x,m} y_0)}{\frac{\sinh(2k_{x,m}a)}{2k_{x,m}} + \frac{\cosh^2(k_{x,m}a)}{\sin^2[k_{y,n}(b-a)]} \left\{ \frac{b-a}{2} \left(\epsilon_r + \frac{k_{y,n}^2}{k_{x,m}^2} \right) - \frac{\sin[2k_{y,n}(b-a)]}{4k_{y,n}} \left(\epsilon_r - \frac{k_{y,n}^2}{k_{x,m}^2} \right) \right\}} \end{aligned} \quad (20)$$

The field amplitudes for the dipole modes can be obtained from the previous equations by substituting $\sinh(k_{x,m}u)$ for $\cosh(k_{x,m}u)$ where u takes on the values of a and y_0 . As expected, the wakefield amplitude scales linearly with the drive bunch charge and inverse proportionally with the transverse size of the structure. To this point this model is fully three-dimensional and the only limitation stems from the assumed symmetry of the transverse drive charge distribution with respect to the y axis.

2.4 COMPARISON WITH THREE-DIMENSIONAL FDTD SIMULATIONS

To evaluate the wakefield associated to a drive bunch, an integration over the full three-dimensional continuous charge distribution must be performed. In practice the integration is replaced by numerical summations of discrete charge distributions similar to those described by Eq. 2. This process is similar to the charge discretization procedure used in standard PIC algorithms . An important feature of this model is that the integration over x -direction is already performed through the Fourier expansion of the charge distribution. For the charge distributions with the considered in this paper, only a few Fourier terms (< 10) are sufficient to obtain an accurate representation of the distribution along the x direction. This is significantly less than the number of grid points in x -direction needed by most PIC codes to evaluate the 3D-collective effects and external fields.

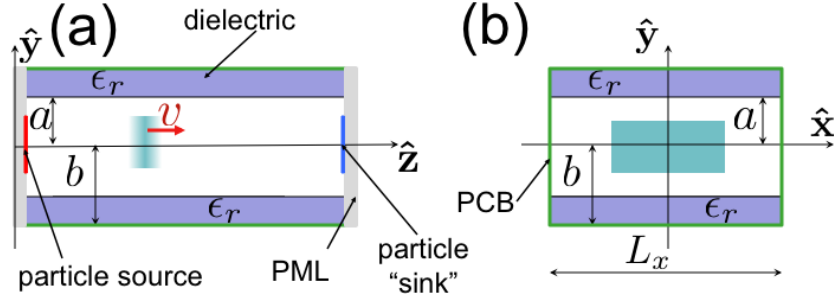


Figure 3: Longitudinal (a) and transverse sections (b) of the DLW model implemented in VORPAL. The rectangular box delimited by green blocks represents the 3D computational domain used in the simulations. Grey, green and purple blocks respectively stand for perfectly-matched layer (PML), perfectly-conducting boundary (PCB), and dielectric material (with associated relative dielectric permittivity ϵ_r). The cyan rectangles represent the electron bunch distribution.

The integration over the vertical direction is straightforward and in most cases, when the drive charge distribution is also symmetric with respect to the horizontal axis, the contribution of the dipole modes cancels out.

Since the phase velocity of the wakefield is the same as the velocity of the drive beam, causality principle requires that the wakefield vanishes ahead of the drive charge. Therefore, the integration over the longitudinal direction extends only from the observation point to the actual drive charge position. The wakefield assumes the form

$$W(z) = \sum_{m=0,1,\dots} \sum_{n=0,1,\dots} \int_z^\infty \rho(z') W_{m,n}(z - z') dz', \quad (21)$$

where W stands for any of the electromagnetic field components and $W_{m,n}$ are the corresponding field component associated to the LSM _{m,n} and LSE _{m,n} modes given respectively by Eq. 14 and Eq. 18. The summation is performed over all modes excited modes.

The results obtained from Eq. 21 are benchmarked against simulations performed with VORPAL a conformal FDTD (CFDTD) PIC electromagnetic solver . VORPAL is a parallel, object-oriented framework for three dimensional relativistic electrostatic and electromagnetic plasma simulation. The DLW model implemented in VORPAL is fully three dimensional; see Fig. 3. The model consists of the rectangular DLW surrounded by perfectly-conducting boundaries (PCBs), The lower and upper z planes are terminated by perfectly matched layers (PMLs) that significantly suppresses artificial reflections of incident radiation . A particle source located on the surface of the lower z plane produced macroparticles uniformly distributed in the transverse plane (x, y) and following a Gaussian longitudinal distribution. The longitudinal Gaussian distribution is truncated at $\pm 3\sigma_z$ where σ_z is its root-mean-square (rms) length. Finally, a “particle sink” at the upper z plane allows macroparticles to exit the computational domain without being scattered or creating other

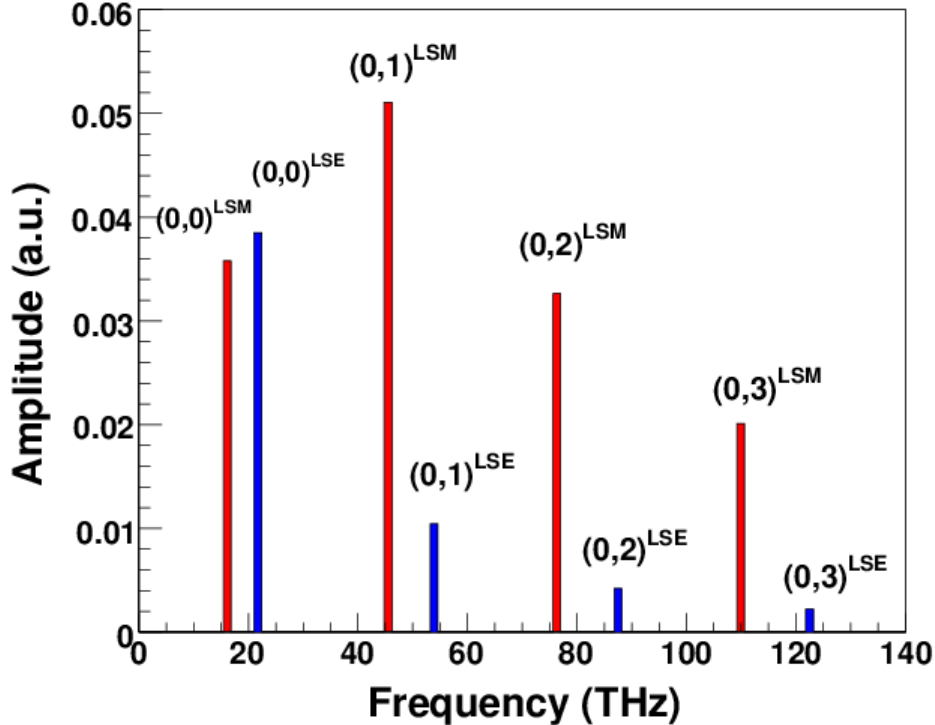


Figure 4: Eigenfrequencies [$f_{m,n} \equiv \omega_{m,n}/(2\pi)$] and associated amplitudes for the mode induced in the DLW with parameter listed in Tab. 1. The (m, n) LSM and LSE modes are respectively shown as red and blue bars .

source of radiation.

In order to precisely benchmark our model, a DLW which support LSM and LSE modes is chosen. The parameters of the structure and driving bunch are gathered in Tab. 1 and the frequency and amplitude associated to the first few modes appear in Fig. 4. The drive-bunch energy is set to $\mathcal{E} = 1.0$ GeV consistently with the ultra-relativistic approximation used in the analytical model.

The longitudinal component of the electric field simulated with VORPAL is shown in Fig. 5 as a two-dimensional projection in the $y - z$ plane.

The comparison between theoretical calculation and VORPAL simulations are shown in Figs. 6 and 7. The fields in Fig. 6 are evaluated as a function of the axial coordinate z at a given transverse location ($x = 3.0$ mm, $y = 2.0$ mm) which corresponds to the upper-left corner of the charge distribution. Figure 7 displays the electromagnetic field evaluated as a function of the horizontal [Fig. 7 (left)] and vertical [Fig. 7 (right)] transverse coordinate at a given axial location $z = 18.6$ mm corresponding to the minimum E_z shown

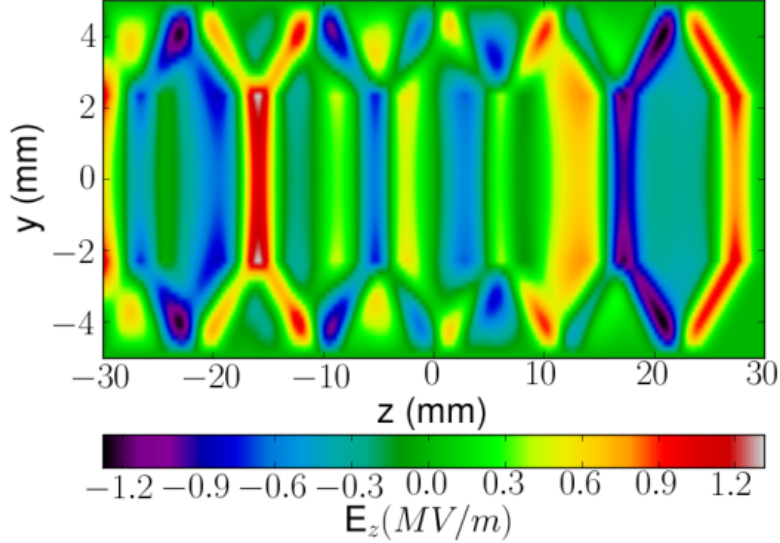


Figure 5: Snapshot of the axial electric field $E_z(x = 0, y, z)$ in the mid-plane of a slab DLW for the bunch and structure parameters shown in Tab. 1. The field was obtained from VORPAL simulations.

in Fig. 6 (i.e. maximum accelerating field). fixed. All plots show a decent agreement (relative discrepancy < 25 %) between our model and VORPAL simulations. The notable disagreement observed in Fig. 6 for the transverse fields in the vicinity of the driving charge (i.e. $z \simeq 27.5$ mm) is rooted in the absence of velocity fields in our model (only radiation field contributes to the wakefield) while the VORPAL simulations include both velocity and radiation fields. In fact given the bunch charge and duration, the amplitude of the velocity field can be evaluated by convolving the charge distribution with the electric field generated by an ultra-relativistic particle $\mathbf{E}(r, \zeta) = 2q(\mathbf{r}_\perp / r_\perp^2)\delta(\zeta)$ where q is the particle's charge and $\mathbf{r}_\perp \equiv (x, y)$ and ζ are respectively the transverse and longitudinal coordinates of the observation point referenced to the particle's location. Such a convolution with our transversely-uniform longitudinally-Gaussian charge distribution yields the electric field at $(x, y, \zeta) = (w_x, w_y, 0)$ to be resulting in a value of ~ 0.8 MV/m for the bunch parameter listed in Tab. 1. The latter value is in agreement with the observed difference between the VORPAL and theoretical models; see E_x and E_y components in Fig. 7.

2.5 TWO-DIMENSIONAL LIMIT

An interesting limiting case occurs when $L_x \gg L_y$. In this “two-dimensional limit”, the dependence of the fields on the horizontal coordinate x is weak and completely vanishes when $L_x \rightarrow \infty$ (so that $k_x \simeq 0$ and $m = 0$). In such a case the field amplitudes associated

Table 1: Parameter of the DLW structure and drive bunch used for benchmarking our theoretical model with VORPAL simulations.

parameter	symbol	value	unit
vacuum gap	a	2.5	mm
height	b	5.0	mm
width	L_x	10.0	mm
relative permittivity	ϵ_r	4.0	--
rms bunch length	σ_z	1.0	mm
bunch charge	Q	1.0	nC
bunch full width	w_x	6.0	mm
bunch full height	w_y	4.0	mm
bunch energy	\mathcal{E}	1	GeV

to the LSM and LSE modes are respectively

$$E_{0;0,n}^{LSM} \simeq \frac{4\Lambda}{a + \frac{\epsilon_r(b-a)}{\sin^2[k_y(b-a)]}}, \text{ and } E_{0;0,n}^{LSE} \simeq 0, \quad (22)$$

where Λ is charge per unit length in the horizontal direction. The LSE modes are suppressed and the latter equation is in agreement with the results of Ref. .

This limit case can be practically reached by using structures with large aspect ratios ($L_x \gg L_y$) driven by flat electron beams (tailored such that $\sigma_x \gg \sigma_y$). Flat beams can be produced in photoinjectors by using a round-to-flat beam transformation . In such a scheme, a beam with large angular-momentum is produced in a photoinjector . Upon removal of the angular momentum by applying a torque with a set of skew quadrupole, the beam has its transverse emittance repartitioned with a tunable transverse emittances ratio . Flat beams with transverse sizes of $\approx 100 \mu\text{m}$ and aspect ratio of ~ 20 have been produced, even at a relatively-low energy of 15 MeV .

Based on the previous experience in producing flat beams and preliminary simulation of the Advanced Superconducting Test Accelerator (ASTA) currently in construction at Fermilab. It is reasonable to consider a 250-MeV 3-nC flat beam generated from a photoinjector to have the following parameters $\sigma_x = XX$, $\sigma_y = 40 \mu\text{m}$, $\sigma_z = 50 \mu\text{m}$. Considering a structure with $a = 100 \mu\text{m}$, $b = 300 \mu\text{m}$ and $\epsilon = 4.5$ would yield a maximum axial wakefield amplitude of $\sim 300 \text{ MV/m}$; see Fig. 8. The fundamental LSM frequency is $f_{1,1} = 193 \text{ GHz}$ and the corresponding LSE mode amplitude is ~ 136 times lower. In Fig. 8 the wakefield is computed with the asymptotic limit provided in Eq. 22 and yet is in excellent agreement with the FDTD simulations.

2.6 IMPLEMENTATION IN A PARTICLE-IN-CELL BEAM DYNAMICS PROGRAM

Although FDTD simulations provide important insight that can aid the design and optimization of the DLW geometry, their use to optimize a whole linear accelerator would be

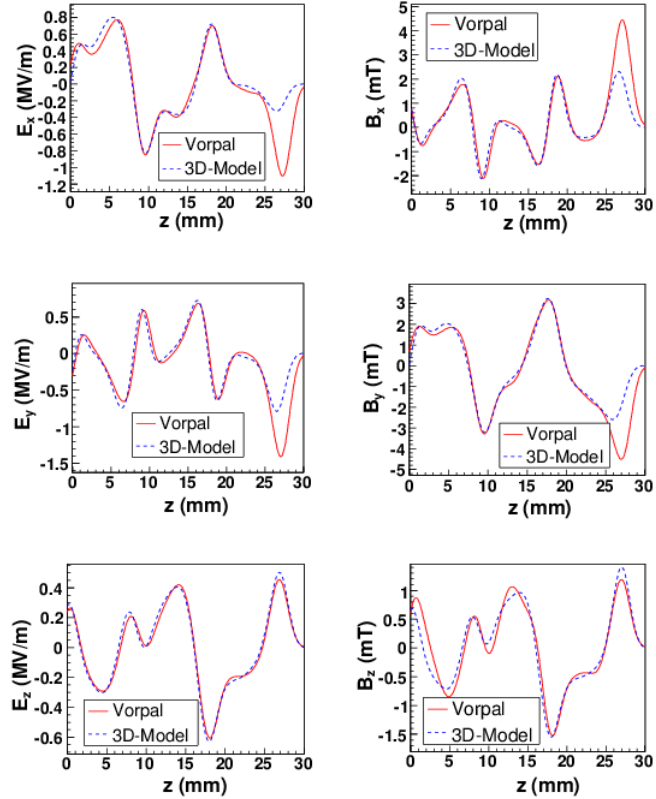


Figure 6: Comparison of the electromagnetic field components calculated with our model (blue dashed line) and simulated with VORPAL (red solid lines). The fields are computed on a line parallel to the z axis with transverse offset $x = 3.0$ mm and $y = 2.0$ mm. The center of the drive beam is at $z = 27.5$ mm. The DLW and bunch parameters are the one displayed in Tab. 1.

time and CPU prohibitive. Therefore it is worthwhile to include a semi-analytical version of the model developed in this paper in a well-established beam dynamics program IMPACT-T. Our main motivation toward this choice stems from the availability of a wide range of beamline elements models. In addition, IMPACT-T takes into account space-charge forces using a three-dimensional electrostatic solver. The algorithm consists in solving Poisson's equation in the bunch's rest frame and Lorentz-boosting the computed electrostatic fields in the laboratory frame.

In a typical particle-tracking PIC program, like IMPACT-T, an electron bunch is described by a set of “macroparticles” with arranged to mimic the bunch phase space distribution. Each macroparticle represents a large number of electrons (typically 10^3 in our simulations). To evaluate the electrostatic fields in the bunch's rest frame the macroparticles are deposited on the cells of a three-dimensional grid.

In order to implement the model described in this paper it is convenient to replace the

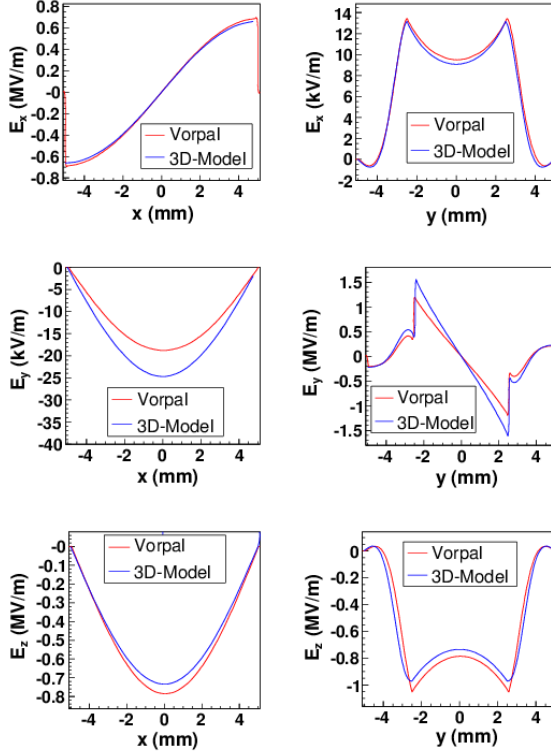


Figure 7: Comparison of the electromagnetic field components calculated with our model (blue dashed line) and simulated with VORPAL (red solid lines). The fields are computed at a given longitudinal position $z = 18.6$ mm. The left-column plots display the dependence on the horizontal coordinate x at $y = 0.043$ mm while the right-column plots show the dependence on the vertical coordinate y at $x = 0.043$ mm. The DLW and bunch parameters are the one displayed in Tab. 1.

Fourier expansion coefficients λ_m from Eq. 2 with discrete charges at the grid nodes. Considering a charge distribution composed two symmetrically located point-charges, $\rho(x) = q[\delta(x - x_0) + \delta(x + x_0)]$ then

$$\lambda_m = \frac{2q|x_0| \cos(k_{x,m}x_0)}{L_x}. \quad (23)$$

In general, the λ_m 's are sums over the nodes with $x > 0$. In practice the sums extend over all nodes provided that the charges located at symmetric nodes are about the same $q_1(x_0) \approx q_2(-x_0)$.

The general expressions of the wakefields at a given position have the following form

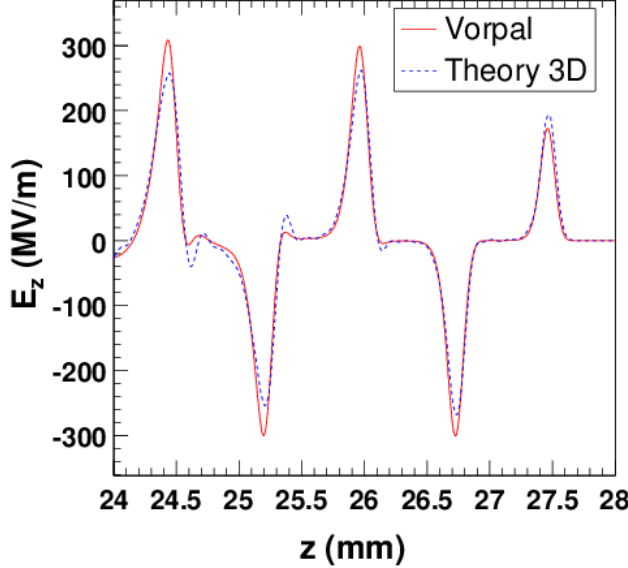


Figure 8: Longitudinal electric field for a DLW with $L_x \gg L_y$ driven by a 3-nC bunch. The bunch has a rectangular transverse shape with full width $w_x = 3.0$ mm and $w_y = 150$ μm , and a Gaussian longitudinal distribution with rms length $\sigma_z = 50$ μm . The theoretical model based on Eq. 22 (dashed blue line) is compared with VORPAL simulations (red line).

$$E_i = \sum_n f_i(x, y; n) \left(\sum_{z_0 > z} \cos [k_z(z_0 - z)] T_i(z_0; n) \right), \quad (24)$$

where $i \equiv x, y, z$, n is the mode index, f_i 's are geometry dependent functions of the type described in Eq. 6 and

$$T_i(z_0; n) = \sum_{x_0, y_0} q|_{x_0, y_0, z_0} \cos(k_{x,m}x_0) \cosh(k_{x,m}y_0). \quad (25)$$

In the latter equation the substitution $\cosh \leftrightarrow \sinh$ should be made when considering dipole modes.

The simulated electromagnetic field components are compared with VORPAL simulations in Fig. 9 for the same case as presented in Fig. 6. In the Fig. 9 the IMPACT-T simulation are performed with and without activating the space-charge algorithm. When accounting for space-charge forces, IMPACT-T is in very good agreement with VORPAL.

The convolution over the z -summation in Eq. 24 can be performed with a numerical Fast Fourier Transformation (FFT). Therefore the total number of operations needed to

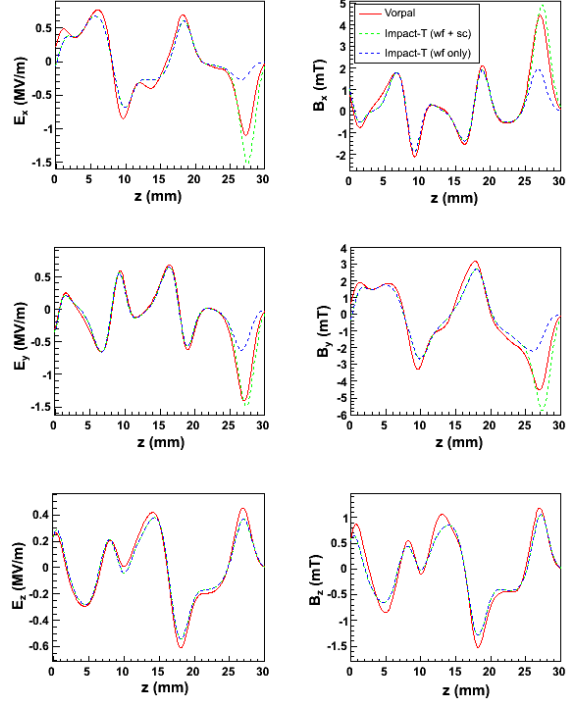


Figure 9: Comparison of the electromagnetic field components obtained from IMPACT T [with (green dashed line) and without (blue dashed line) accounting for space charge forces] with the fields simulated with VORPAL (red solid lines). The fields are computed on a line parallel to the z axis with transverse offset $x = 3.0$ mm and $y = 2.0$ mm. The center of the drive beam is at $z = 27.5$ mm. The DLW and bunch parameters are the one displayed in Tab. 1.

evaluate the wakefields is $\propto N_{modes} N_x^2 N_y^2 N_z \log N_z$. The total number of modes is twice the product between the modes allowed for each of the transverse wave numbers: $N_{modes} = 2N_{k_x}N_{k_y}$. The factor of 2 comes from the inclusion of the dipole modes along with the vertically symmetric monopole modes. For the data generated in Fig. 9, the IMPACT-T simulations are more than two orders of magnitude faster than the VORPAL ones.

3 ELECTRON-BUNCH SHAPING FOR ENHANCED TRANSFORMER RATIO

3.1 TRADEOFFS BETWEEN TRANSFORMER RATIO AND PEAK ACCELERATING FIELD

The maximization of \mathcal{R} has been well studied and can be achieved by making the decelerating field constant over the drive bunch. In contrast, the maximization of E_+ can be achieved by maximizing the peak current. This however, produces a very large E_- which effectively reduces \mathcal{R} . We consequently investigated the relationship between E_+ and \mathcal{R} for different current shapes. The six shapes considered are as follows:

- Gaussian distribution: $g(x) = \frac{1}{\sqrt{2\pi}\sigma} e^{-(z-\mu)^2/(2\sigma^2)}$, where μ and σ are the mean and root-mean-square (rms) length,
- Linearly-ramped: $g(z) = mz + b$, with m and b as parameters,
- Fourier distribution: $g(z) = \sum_{n=1}^5 b_n \sin(nz)$ where b_n 's are free parameters,
- Double triangle distribution as a combination of two linearly-ramped distribution parametrized by l_n and h_n , the horizontal and vertical position of the n -th vertice respectively.
- Exponential distribution: $g(z) = e^{-\alpha z}$ for $z \in [0, L]$ with α and L as parameters,
- Skewed gaussian distribution: $g(z) = \frac{2}{\omega} \phi\left(\frac{z-\xi}{\omega}\right) \Phi\left(\alpha\left(\frac{z-\xi}{\omega}\right)\right)$, where ξ is a shift, ω the characteristic length, and α the skew, $\phi(x) = \frac{1}{\sqrt{2\pi}} e^{-\frac{x^2}{2}}$, and $\Phi(x) = \frac{1}{2} \left[1 + \text{erf}\left(\frac{x}{\sqrt{2}}\right)\right]$,
- “Realistic” current achievable with longitudinal-phase-space manipulation $g(z) = \int d\tilde{z} I_f^u(\tilde{z}) \exp\left[-\frac{(z-\tilde{z})^2}{2\sigma_u^2}\right]$, where $I_f^u(z) = \frac{\hat{I}_0}{\Delta^{1/2}(z)} \exp\left[-\frac{(a_f + \Delta^{1/2}(z))^2}{8b_f^2 \sigma_{z,0}^2}\right] \times \Theta[\Delta(z)]$, with $\Delta(z) \equiv a_f^2 + 4b_f z$ and $\Theta()$ is the Heaviside function. The final current shape is therefore controlled via the parameters a_f and b_f . Here we take $\sigma_u = 0.05$.

Typical shapes associated to these functions $g(z)$ are displayed in Fig. 10 (left). Once a set of parameters is selected, the corresponding distribution is normalized to i.e. unity as $\bar{g}(z) = \frac{g(z)}{\int_{-\infty}^{+\infty} g(z) dz}$. The bunch charge is then set to $Q = 1$ nC to yield the current profile $I(z) = Qc\bar{g}(z)$ where c is the velocity of light.

3.1.1 SIMULATION METHODS

In order to explore the performances of the current profiles in beam-driven dielectric-wakefield acceleration, we considerer a diamond DLW with parameters listed in Tab. 2. Given the current profile $I(z)$, the axial electric field is computed as the integral

$$E(z) = \sum_n \int_{-\infty}^z I(z - \tilde{z}) W_n(\tilde{z}) d\tilde{z} \quad (26)$$

where $W_n(z)$ are the Green's functions associated to the n^{th} mode; see Ref. . For our calculation with limit the summation to $n = 4$ modes. Once the axial field is obtained the decelerating field is computed as $E_- = \max[E(z)]$ for z within the bunch and $E_+ = \min[E(z)]$ for z behind the bunch.

Table 2: Parameters associated to the dielectric structure used in the wakefield simulations.

Distribution	Parameters	Units
inner radius a	165	μm
outer radius b	195	μm
relative permittivity ϵ_r	5.7	–
fundamental frequency f_0	0.83	THz

These semi-analytical simulations were imbedded in a genetic optimizer . For each current profile, the associated parameters were varied. The two goals of the optimizer are to find parameters that maximize E_+ and \mathcal{R} .

3.1.2 RESULTS

Each shape was optimized over the parameters listed above respectively. Bunch shapes with a small number of parameters (e.g. gaussian and ramped bunch) converged more quickly than more complicated shapes (e.g double triangle, skewed gaussian, "realistic" parameterization). On average, approximately 15,000 runs were done per shape. The best achieved values for \mathcal{R} and E_+ are summarized in Fig. 10 (right).

We clearly see a trade-off between \mathcal{R} and E_+ : as expected, current profiles resulting in large \mathcal{R} are restricted to smaller values of E_+ and vice versa. The data presented in Fig. 10 was generated using a 1-nC electron bunch; increasing the charge would result in higher E_+ without affecting \mathcal{R} . Interestingly, none of the asymmetric shapes investigated stand out as a best candidate. A linear regression of the best cases provides an empirical limit for the maximum value of \mathcal{R} : $\max[\mathcal{R}] \sim 400 \times E_+^{-0.8}$. For the chosen structure parameters, value of $\mathcal{R} > 10$ are achieved with $E_+ \approx 100 \text{ MV/m}$. Again, increasing the charge to, e.g., 5-nC would result in 0.5-GV/m field or alternatively could enable reaching higher transformer ratio values for 100-MV/m fields as done in Ref. . In DLW-based acceleration, larger E_+ values could also be reached by reducing the aperture of the structure.

For the chosen structure parameters, value of $\mathcal{R} > 10$ are achieved with E_+ in the vicinity of 100 MV/m for 1-nC. Increasing the charge to, e.g., 5 nC would results in 0.5 GV/m field or alternatively could enable reaching higher transformer ratio value for 100-MV/m fields.

In Figures. 11 and 12 we present an example of optimized Fourier and skew-Gaussian distributions, both have $\mathcal{R} > 6$ and $E_+ > 150 \text{ MV/m}$. In Fig. 12 a skewed gaussian excites a wakefield with a nice high \mathcal{R} . An important aspect of the skew-Gaussian distribution on this example is its ability to provide a slightly flattened accelerating field over the prospective location of a witness bunch. This latter feature, also observed for the double-triangle distribution, would reduce the energy spread imparted on the witness bunch.

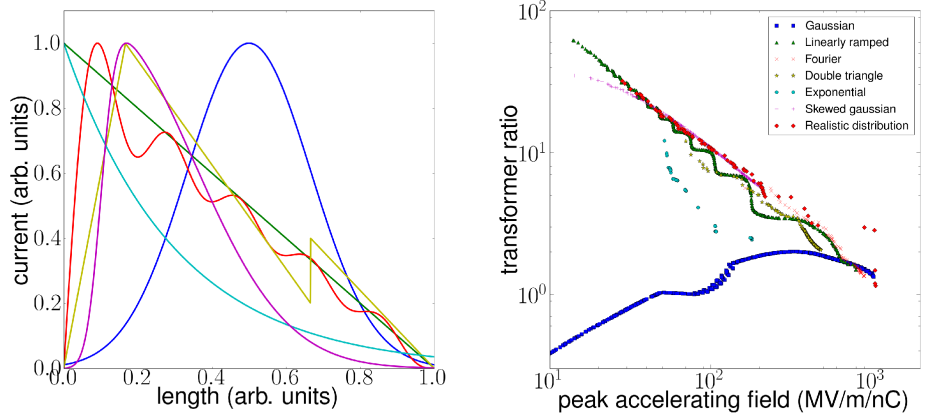


Figure 10: Shapes considered in our study: Gaussian (blue), linearly-ramped (green), exponential (cyan), Fourier (red), double triangle (yellow), and skewed gaussian (magenta) (left) and trade-off curve between \mathcal{R} and E_+ for the different shapes shown in the left plot with same color coding (right). The axis of the left plot are normalized to unity for clarity, e.g., the traces shown correspond to $g[z/\max(z)]/\max[g(z)]$.

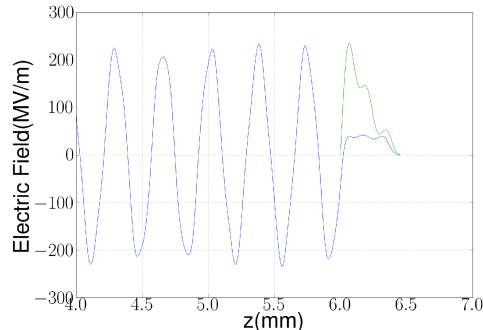


Figure 11: Fourier distribution (green trace) and associated wakefield (blue trace).

Finally, we present an example of wakefield generated by the “realistic” bunch in Fig. 12. Such a bunch shape is achievable using a dual-frequency linear accelerator which will be used in a forthcoming experiment to demonstrate beam-driven acceleration with a enhanced transformer ratio .

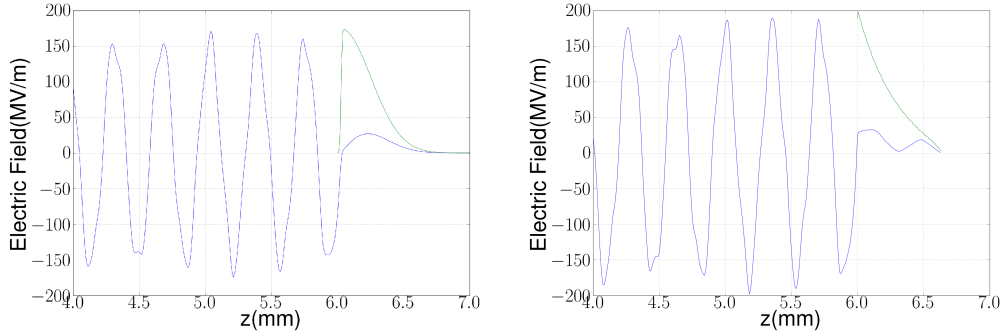


Figure 12: Skewed-Gaussian (left) and “realistic” (experimentally measured) distributions (right) (green trace) and associated wakefields (blue trace).

3.2 OPTIMUM ELECTRON-BUNCH SHAPE

In beam driven techniques, a “drive” bunch passes through a high-impedance medium and experiences a decelerating field. The resulting energy loss can be transferred to a properly delayed “witness” bunch trailing the drive bunch in the medium. The transformer ratio, defined as $\mathcal{R} = E_+/E_-$ [where E_+ (reps. E_-) is the maximum accelerating (reps. minimum decelerating) field behind (reps. within) the drive bunch] is an important figure of merit as it describes the energy transfer within the two bunches. For symmetric bunches, $\mathcal{R} \leq 2$. Going beyond $\mathcal{R} = 2$ requires asymmetric bunches and can be maximized by generating a flat decelerating field over the drive bunch; however, increasing \mathcal{R} generally reduces E_+ and the relationship between them is left to a compromise .

In practice however, the acceleration gradients and acceleration frequencies depend on the interaction medium, which for e.g. dielectric wakefield acceleration, depend on the dimensions of the structure. Therefore altogether, the structure dimensions are also limited by the beam properties such as the beam energy and beta functions. At low energy for example, due to the difficulty of fitting into relatively long structures, it is more valuable to excite high-gradient wakes with shorter bunches with poor transformer ratios. On the other hand, high energy beams with relatively smaller betatron functions can fit into much longer, and smaller structures. In this perspective it is more useful to drive wakes efficiently with high transformer ratios.

To date, several current profiles capable of generating optimal transformer ratios have been proposed. These include linearly ramped profiles combined with a door-step or exponential initial distribution , and more recently the double-triangle current profiles . In general, these shapes present discontinuities and rely on complicated beam manipulation techniques which have limited applications .

During our research we introduce a new class of smooth current profiles which also lead to constant decelerating fields across the drive bunch to lead to optimal transformer ratios. We also discuss a possible scheme for realizing these shapes employing a shaped

photocathode-laser pulse.

For simplicity we consider a wakefield structure that supports an axial wakefield described by the Green's function

$$G(z) = 2\kappa \cos(\omega_0 z/c), \quad (27)$$

where κ is the loss factor and $\omega_0 \equiv 2\pi c/\lambda$ with λ being the wavelength of the considered mode. Here z is the distance behind the source particle responsible for the wakefield. We do not specialize to any particular wakefield mechanism and depending on the structure used many modes might be excited so that the Green's function would consist of a summation over these modes.

3.2.1 SMOOTH CURRENT PROFILES FOR ENHANCED TRANSFORMER RATIOS

Optimal- \mathcal{R} shapes are useful for generating flat decelerating fields over the bunch; this inherently reduces the energy spread incurred over the bunch. Additionally, these shapes lead to the most efficient energy transfer between a drive and witness bunch which could lead to overall higher witness bunch energies.

Based on the work presented in Ref. , we consider a bunch-current profile described as a piecewise function $I(t)$. We take $I(t)$ to be piecewise on two intervals $[0, \tau]$ and $[\tau, T]$ and zero elsewhere. Also we constrain our search to functions such that $I(t)$ and $\dot{I}(t) \equiv dI/dt$ are continuous at $t = \tau$.

As an example we consider a modulated linear ramp function over $[0, \tau]$ of the form

$$s(t) = at + b \sin(\omega t), \quad (28)$$

where a and b are constant, and ω_0 is the modulation frequency. We correspondingly introduce the current profile as the piecewise (continuous) function

$$I(t) = I_0 \begin{cases} s(t) & \text{if } 0 \leq t < \tau, \\ s'(\tau)t - s'(\tau)\tau + s(\tau) & \text{if } \tau \leq t \leq T, \\ 0 & \text{elsewhere.} \end{cases} \quad (29)$$

where I_0 is the peak current. An example of current shape is depicted in Fig. 13 (a).

We further specialize, for simplicity, to the case where $\tau = 2n\pi/\omega$ (where $n \in \mathbb{N}$) and $\omega_0 = \omega/q$ (where ω_0 is defined in Eq. 27 and $m \in \mathbb{N}$) The decelerating field (V^-) over the drive bunch is found to be

$$V^-(t) = I_0 \begin{cases} -\frac{q^2}{\omega^2(q^2-1)} \left([aq^2 - (b\omega + a)] \cos \frac{\omega t}{q} + b\omega \cos \omega t - a(q^2 - 1) \right) & \text{if } 0 \leq t < \tau, \\ -\frac{q^2}{\omega^2(q^2-1)} \left(b\omega q^2 \cos \frac{\omega t - 2\pi n}{q} + [aq^2 - (b\omega + a)] \cos \frac{\omega t}{q} + (b\omega + a)(1 - q^2) \right) & \text{if } \tau \leq t < T, \\ 0 & \text{elsewhere.} \end{cases} \quad (30)$$

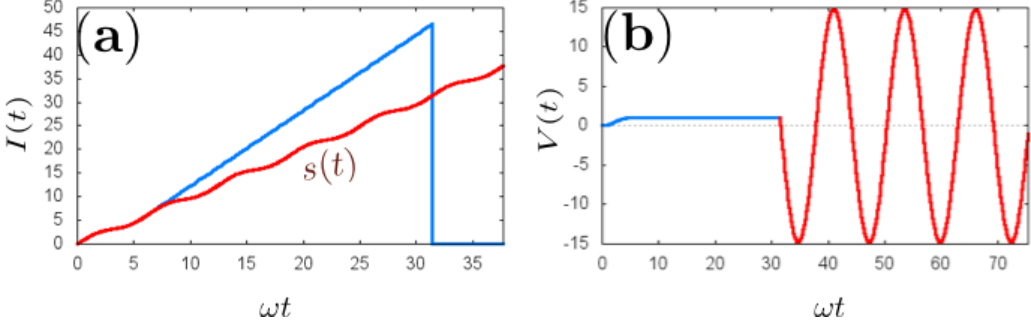


Figure 13: Example (a) of current profile (blue trace) described by Eq. 29 (a) and $s(t)$ function (red trace). The corresponding induced voltage (b) within (blue trace) and behind (red trace) the bunch. For these data $I_0 = 1$, $a = 1$, $b = 3a/5$, $n = 1$, $m = 5$ and $q = 2$. (the current and voltage units are arbitrary).

The above equation shows that when $\frac{n}{q} = \frac{l}{2}$ (where $l \in \mathbb{N}$), the decelerating field is constant for $t \in [\tau, T]$ and can be written

$$V_{t \in [\tau, T]}^-(t) = \frac{-I_0 q^2}{\omega^2 (q^2 - 1)} \left([b\omega((-1)^{\frac{2n}{q}} q^2 - 1) + a(q^2 - 1)] \cos \frac{\omega t}{q} + (b\omega + a)(1 - q^2) \right), \quad (31)$$

so that the time dependence of the decelerating potential can be cancelled by choosing the ramp parameters a and b to satisfy the equation

$$b = \frac{a(1 - q^2)}{\omega[(-1)^{\frac{2n}{q}} q^2 - 1]}. \quad (32)$$

Specializing to the case where $2n/q$ is an odd number gives $b = a(q^2 - 1)/[\omega(1 + q^2)]$ and the decelerating voltage across the bunch takes the form

$$V^-(t) = I_0 \begin{cases} \frac{aq^2 I_0}{\omega^2(1+q^2)} \left(q^2 \cos \frac{\omega t}{q} + a \cos \omega t - (1 + q^2) \right) & \text{if } 0 \leq t < \tau, \\ \frac{2aI_0q^4}{\omega^2(1+q^2)} & \text{if } \tau \leq t < T, \\ 0 & \text{elsewhere.} \end{cases} \quad (33)$$

The latter case is illustrated in Fig. 13 (b) with $l \equiv n/q = 1/2$. Likewise the induced oscillating voltage behind the bunch can be obtained from

$$V^+(t) = \frac{aq^2 I_0}{\omega^2(1+q^2)} \left(\pi[q^2(1 - 2m) - 1] \sin \left(\frac{\omega t}{q} - \pi m \right) + 2q^2 \cos \left(\frac{\omega t}{q} - \pi m \right) \right) \quad (34)$$

The second term can be dropped to good approximation to find a lower estimate on the transformer ratio, without loss of generality

$$\mathcal{R} = \left(m + \frac{1 - q^2}{2q^2} \right) \pi, \quad (35)$$

where m is the number of the fundamental-mode wavelengths within the total bunch length. We note that for short bunch durations (i.e. as needed to produce high accelerating fields), the latter transformer ratio is higher than other proposed distributions.

3.2.2 BEAM SHAPING USING A TAILORED PHOTOCATHODE LASER

To date, longitudinal shaping for enhanced transformer ratios has only been demonstrated using a mask in a dispersive section. Another proposed technique relies on using a mask to shape a beam transversely, and use an emittance exchanger to rotate the shape longitudinally. In the former case, the scheme is limited to specific shapes in the mask, and inherits beam losses. Additionally shapes which require sharp edges (e.g. double-triangle) are limited by the dispersion and emittance of the beam at the mask. The latter scheme requires a deflection cavity in a dispersive section which complicates the overall procedure; moreover, this scheme also inherits beam losses from a mask upstream, and is also limited by beam emittances.

An alternative approach is to longitudinally tailor the laser profile in a high-gradient photoinjector. In such a scenario, electrons emitted from the photocathode will have an initial longitudinal distribution similar to the injected laser pulse. We consider an example of an S-Band gun operating at 140 MV/m to reduce the space-charge effects. Generally higher accelerating fields in a gun lead to higher charge densities which could drive larger gradient wakefields inside DLWs. We use the particle-tracking program *astra* which takes into account space charge effects using a cylindrical-symmetric algorithm . We model the 1-nC electron bunch considered in our studies with 50,000 macroparticles. Additionally the laser is chosen to have a transverse rms spot size of $\sigma_c = 0.8$ mm and rms duration of $\sigma_t = 1$ ps. A solenoidal lens is placed downstream of the gun to maintain the transverse size below 1 cm over a drift length of 1 m.

In general, photoemission is a intricate process which depends on many parameters including the amplitude and phase (with respect to the laser) of the applied accelerating field on the photocathode surface, the bunch charge, and the cathode material properties. It is challenging to analytically find an optimum laser shape that provide a given current distribution at a given location. Work toward the production of ramped current profile was investigated in the context of seeded free-electron laser research and experimentally demonstrated at the FERMI facility . Additionally, we demonstrated that a passive technique employing a wakefield structure combined with a non-ultra-relativistic bunch could produce ramped bunch.

Therefore to explore the production of tailored electron bunches using temporally-shaped photocathode laser pulses, we carry numerical simulation using the ASTRA particle tracking program . and explored the outcome of various shapes. In this section we report on the performance of the exponential distribution given by:

$$f(t) = f_0(e^{\mu t} - 1)H(\theta - t), \quad (36)$$

where μ is a growth rate and θ is the ending time of the pulse $H(t)$ is the Heaviside function. The laser intensity f_0 has to be normalized to produce the required bunch charge after the photo-emission process. We consider three case of exponentially-shaped laser distributions.

All have a total pulse duration of $\theta = 5$ ps but different steepness characterized by a growth rate $\mu = 3.90 \times 10^5, 6.92 \times 10^5, 1.00 \times 10^6$; see Fig. 14 (upper-right plot).

The growth rate μ primarily influences the electrostatic field inside the bunch which affects the final longitudinal phase space. The case of large growth rate yield the formation of ellipsoidal distribution via the blow-out regime. In the limit of small growth rates, the laser profile become linearly ramped but the ramp quickly dissipates. Figure 14 (upper right, and lower row plots) displays snapshots of the the longitudinal phase spaces and associated current distribution for the three case of growth rate mentioned.

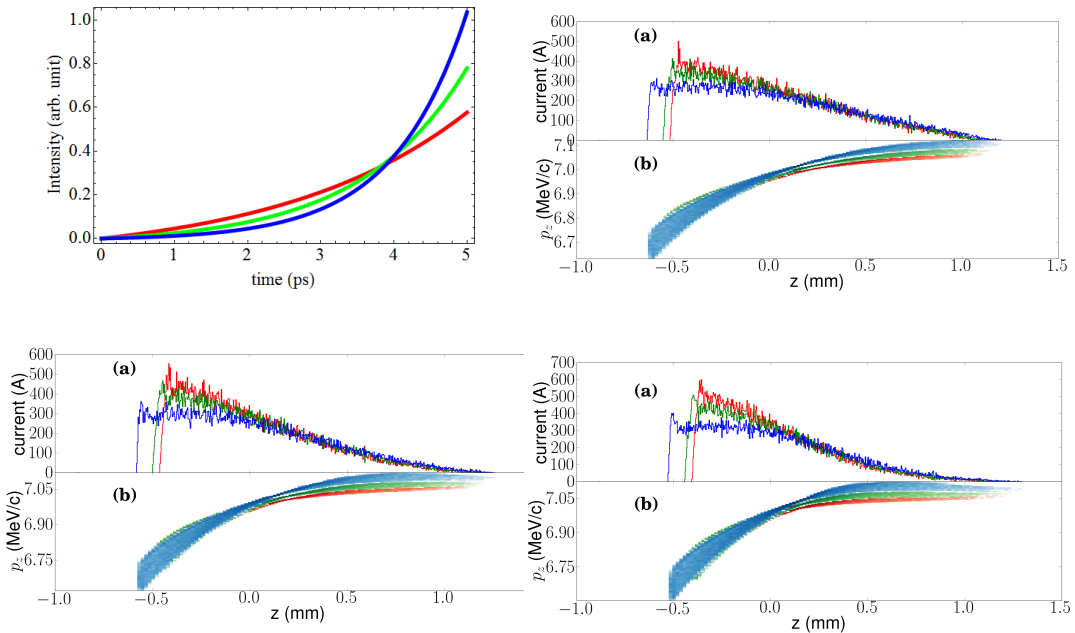


Figure 14: Initial photocathode laser pulse temporal distributions (top left) and snapshots of the current (a) and longitudinal phase space (b) at 25 cm (red), 50 cm (green), 100 cm (blue) from the photocathode. The top-right, lower-left and lower-right plots correspond respectively to the initial laser distributions appearing as a red, green, and blue trace (with increasing steepness) in the top-left plot.

Finally, we quantify the capability of the formed electron bunches to serve as a wake-field drive by considering their applications to drive wakefield in a dielectric structure. We therefore convolve the shapes with the one-dimensional Green's function associated to a cylindrically-symmetric dielectric-line waveguide (DLW) . We choose a DLW with inner radius $a = 165 \mu\text{m}$, outer radius $b = 195 \mu\text{m}$, and relative dielectric permittivity $\epsilon = 5.7$; here we note that in order to fit the beam into a structure with such dimensions would require a significant increase in beam energy which could also “freeze” the evolution of the beam. For the three cases, we record E_+ and \mathcal{R} along the drift following the photocathode, the results are shown in Fig. 15. The results indicate that both large E_+ and \mathcal{R} are

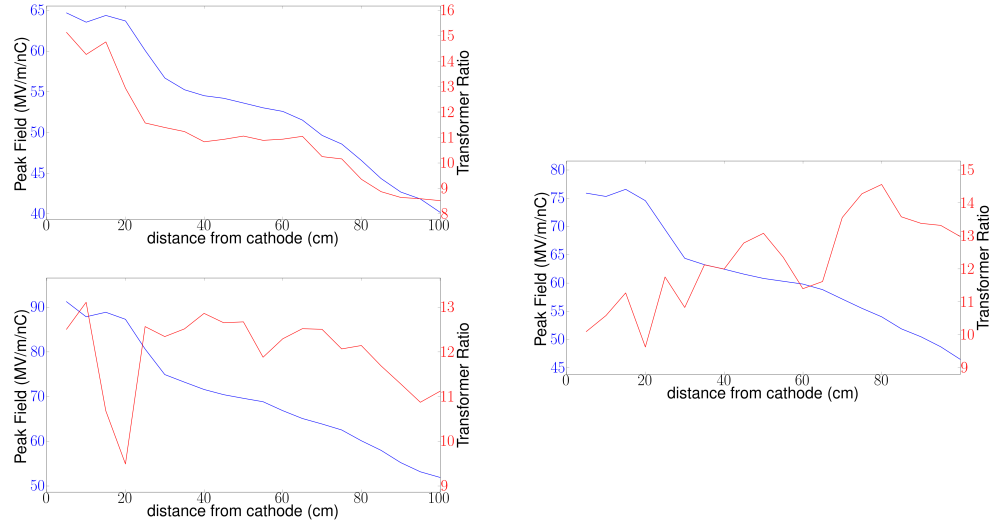


Figure 15: The calculated E_+ (blue trace) and \mathcal{R} (red trace) as a function of drift length from the photocathode in a DLW with dimensions described above. The top left, right, and bottom left plots correspond to initial exponential distributions red, green, blue shown in Fig. 14 (top left) respectively.

achievable for the different laser distribution along the beamline. The variation parameter μ adds some flexibility between large E_+ and R and generally larger μ lead to larger E_+ . Although in our examples, the bunch shape is still evolving, it could in principle be possible to add a booster cavity and optimize the setup to ensure the optimum shape is formed downstream of the booster cavity at a sufficiently high energy to freeze the longitudinal motion within the bunch.

3.3 EXPERIMENTAL REALIZATION OF A LINEARLY-RAMPED BUNCH WITH A MULTIFREQUENCY LINAC

We first elaborate the proposed method using a 1D-1V single-particle model of the LPS dynamics and take an electron with coordinates (z, δ) where z refers to the longitudinal position of the electron with respect to the bunch barycenter (in our convention $z > 0$ corresponds to the head of the bunch) and $\delta \equiv p/\langle p \rangle - 1$ is the fractional momentum error (p is the electron's momentum and $\langle p \rangle$ the average momentum of the bunch). Considering a photo-emission electron source, the LPS coordinates downstream are $(z_0, \delta_0 = a_0 z_0 + b_0 z_0^2 + \mathcal{O}(z_0^3))$ where a_0 , and b_0 are constants that depend on the bunch charge and operating parameters of the electron source. For sake of simplicity we limit our model to second order in z_0 and δ_0 . Next, we examine the acceleration through a linac operating at the frequencies f_1 and $f_n \equiv n f_1$ with total accelerating voltage $V(z) = V_1 \cos(k_1 z + \varphi_1) + V_n \cos(k_n z + \varphi_n)$ where $V_{1,n}$ and $\varphi_{1,n}$ are respectively the accelerating voltages and operating phases of the two linac sections, and $k_{1,n} \equiv 2\pi f_{1,n}/c$. In our convention, when the phases between the linac sections and the electron bunch are $\varphi_{1,n} = 0$ the bunch energy gain is maximum (this is refer to as on-crest operation). Under the assumption $k_{1,n} z_0 \ll 1$ and neglecting non-relativistic effects, the electron's LPS coordinate downstream of the linac are $(z_l = z_0, \delta_l = a_l z_0 + b_l z_0^2)$ where $a_l \equiv a_0 - e(k_1 V_1 \sin \varphi_1 + k_n V_n \sin \varphi_n)/\bar{E}_l$, $b_l \equiv b_0 - e(k_1^2 V_1 \cos \varphi_1 + k_n^2 V_n \cos \varphi_n)/(2\bar{E}_l)$ with e being the electronic charge and \bar{E}_l the beam's average energy downstream of the linac. Finally, we study the passage of the bunch through an achromatic current-enhancing dispersive section [henceforth referred to as "bunch compressor" (BC)]. The LPS dynamics through a BC is approximated by the transformation $z_f = R_{56} \delta_l + T_{566} \delta_l^2$ where R_{56} (also referred to as longitudinal dispersion), and T_{566} are the coefficients of the Taylor expansion of the transfer map $\langle z_f | \delta_l \rangle$ of the BC. Therefore the final position is given as function of the initial coordinates following $z_f = a_f z_0 + b_f z_0^2$ with $a_f \equiv 1 + a_l R_{56}$ and $b_f \equiv b_l R_{56} + a_l^2 T_{566}$. Taking the initial current to follow the Gaussian distribution $I_0(z_0) = \hat{I}_0 \exp[-z_0^2/(2\sigma_{z,0}^2)]$ (where \hat{I}_0 is the initial peak current), and invoking the charge conservation $I_f(z_f) dz = I_0(z_0) dz_0$ gives the final current distribution $I_f^u(z_f) = \hat{I}_0 / \Delta^{1/2}(z_f) \exp[-(a_f + \Delta^{1/2}(z_f))^2/(8b_f^2 \sigma_{z,0}^2)] \Theta[\Delta(z_f)]$ where $\Delta(z_f) \equiv a_f^2 + 4b_f z_f$ and $\Theta()$ is the Heaviside function. The latter current distribution does not include the effect of the initial uncorrelated fractional momentum spread $\sigma_{\delta,0}^u$. The final current, taking into account $\sigma_{\delta,0}^u$, is given by the convolution $I_f(z_f) = \int d\tilde{z}_f I_f^u(\tilde{z}_f) \exp[-(z_f - \tilde{z}_f)^2/(2\sigma_u^2)]$ where $\sigma_u \equiv R_{56} \sigma_{\delta,0}^u$. The final current shape is controlled via a_f and b_f and can be tailored to follow a linear ramp as demonstrated in Fig. 16.

The experiment described in this Letter was performed at the Free-electron LASer in Hamburg (FLASH) facility . In the FLASH accelerator, diagrammed in Fig. 17, the electron bunches are generated via photoemission from a cesium telluride photocathode located on the back plate of a 1+1/2 cell normal-conducting rf cavity operating at 1.3 GHz on the TM₀₁₀ π -mode (rf gun). The bunch is then accelerated in a 1.3-GHz and 3.9-GHz superconducting accelerating modules (respectively ACC1 and ACC39) before passing through a bunch compressor (BC1). The ACC39 3rd-harmonic module was installed to nominally correct for nonlinear distortions in the LPS and enhance the final peak current

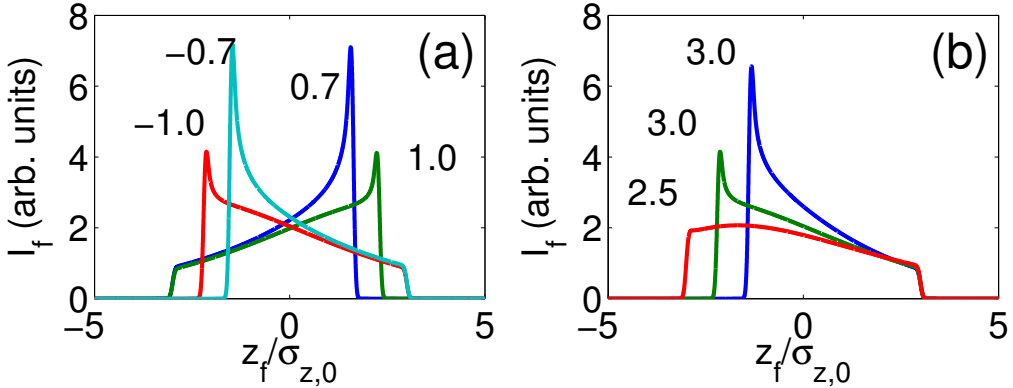


Figure 16: Analytically-computed current profiles for several values of b_f for fixed $a_f = 2.5$ (a) and for several values of a_f with $b_f = 0.7$ (b). The numbers in (a) [resp. (b)] are the values of b_f [resp. a_f]; for all the cases $\sigma_u = 0.05$.

of the electron bunch . Downstream of BC1, the bunch is accelerated and can be further compressed in BC2. A last acceleration stage (ACC4/5/6/7) brings the beam to its final energy (maximum of ~ 1.2 GeV). The beam's direction is then horizontally translated using a dispersionless section referred to as dogleg beamline (DLB). Nominally, the beam is sent to a string of undulators to produce ultraviolet light via the self-amplified stimulated emission free-electron laser (FEL) process. For our experiment, the bunches were instead vertically sheared by a 2.856-GHz transverse deflecting structure (TDS) operating on the TM₁₁₀-like mode and horizontally bent by a downstream spectrometer . Consequently the transverse density measured on the downstream Cerium-doped Yttrium Aluminum Garnet (Ce:YAG) scintillating screen is representative of the LPS density distribution. The horizontal and vertical coordinates at the Ce:YAG screen are respectively $x_s \simeq \eta\delta_F$, where $\eta \simeq 0.75$ m is the horizontal dispersion function, and $y_s \simeq \kappa z_F$ where $\kappa \simeq 20$ is the vertical shearing factor and (z_F, δ_F) refers to the LPS coordinate upstream of the TDS. The exact values of η and κ are experimentally determined via a beam-based calibration procedure.

The accelerator parameters settings are gathered in Tab. 3. The nominal settings of BC2 were altered to reduce its longitudinal dispersion $R_{56}^{(2)}$ and the ACC2/3 and ACC4/5/6/7 accelerating modules were operated on crest. Such settings insure that the BC2 and the DBL sections do not significantly affect the LPS beam dynamics. Therefore the measured current profile is representative of the profile downstream of BC1.

In order to validate the simple analytical model described above, numerical simulations of the LPS beam dynamics were carried using a multi-particle model. The simulations also enable the investigation of possible detrimental effects resulting from collective effects such as longitudinal space charge (LSC) and beam self interaction via coherent synchrotron radiation (CSR) . In these simulations, the beam dynamics in the rf-gun was modeled with the particle-in-cell program ASTRA and the obtained distribution was subsequently tracked in the accelerating modules using a 1D-1V program that incorporates a one-dimensional

Table 3: Settings of accelerator subsystems relevant to the LPS dynamics used in the experiment and simulations.

parameter	symbol	value	unit
ACC1 voltage	V_1	[140-157]	MV
ACC1 phase	φ_1	[-10,10]	deg
ACC39 voltage	V_3	[13,21]	MV
ACC39 phase	φ_3	[160-180]	deg
ACC2/3 voltage	$V_{1,2-3}$	311	MV
ACC2/3 phase	$\varphi_{1,2-3}$	0	deg
ACC4/5/6/7 voltage	$V_{1,4-7}$	233.9	MV
ACC4/5/6/7 phase	$\varphi_{1,4-7}$	0	deg
BC1 longitudinal dispersion	$R_{56}^{(1)}$	~ 170	mm
BC2 longitudinal dispersion	$R_{56}^{(2)}$	~ 15	mm
Single-bunch charge	Q	0.5	nC
Bunch energy	E	~ 690	MeV

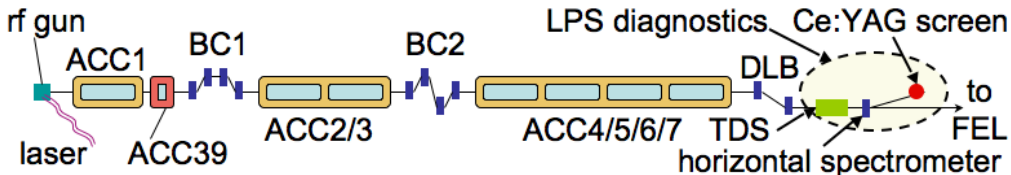


Figure 17: Diagram of the FLASH facility. Only components affecting the longitudinal phase space beam (LPS) dynamics of the bunches are shown. The acronyms ACC, BC, and DBL stand respectively for accelerating modules, bunch compressors, and dogleg beamline (the blue rectangles represent dipole magnets). The transverse deflecting structure (TDS), spectrometer and Ce:YAG screen compose the LPS diagnostics.

model of the LSC. The program CSRTRACK , which self-consistently simulates CSR effects, was used to model the beam dynamics in the BC1, and BC2 sections. An example of simulated LPS distributions and associated current profiles computed for different settings of ACC1 and ACC39 parameters appear in Fig. 18. The results indicate that the production ramped bunches is possible despite the intricate LPS structures developing due to the collective effects and higher-order nonlinear effects not included in our analytical model. The simulations also confirm that the current profile upstream of the TDS (as measured by the LPS diagnostics) is representative of the one downstream of BC1.

Figure 19 displays examples of measured LPS distributions with associated current profiles obtained for different settings of ACC1 and ACC39. As predicted, the observed current profiles are asymmetric and can be tailored to be ramped with the head of the

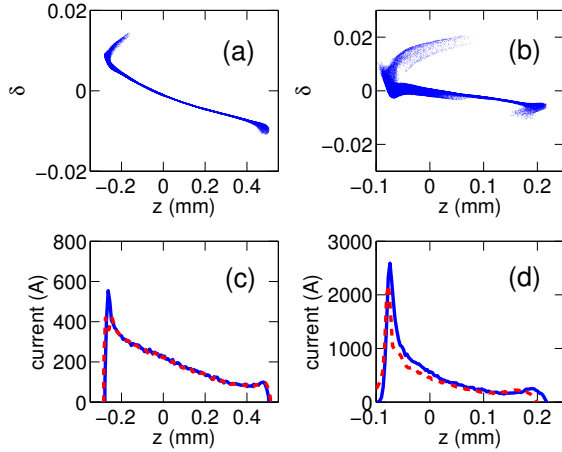


Figure 18: Simulated LPS distribution [(a) and (b)] with associated current profile downstream of BC1 (solid blue trace) and DBL (dash red trace) [(c) and (d)]. The set of plots [(a), (c)] and [(b), (d)] correspond to different $(V_{1,3}, \varphi_{1,3})$ settings.

bunch ($z > 0$) having less charge than the tail; see Fig. 19 (b-d). The latter feature is in contrast with the nominal compression case at FLASH where the LPS distortion usually results in a low-charge trailing population as seen in Fig. 19 (a).

We now quantify the performance of the produced current profiles to enhance beam-driven acceleration techniques by considering a drive bunch injected in a cylindrical-symmetric dielectric-lined waveguide (DLW) . The DLW consists of a hollow dielectric cylinder with inner and outer radii a and b . The cylinder is taken to be diamond (relative electric permittivity $\epsilon_r = 5.7$); and its outer surface is contacted with a perfect conductor; see Fig. 20 (a). The measured current profiles are numerically convolved with the Green’s function associated to the monopole mode to yield the axial electric field . These semi-analytical calculations were benchmarked against finite-difference time-domain electromagnetic simulations executed with VORPAL . The transformer ratio is numerically inferred as $\mathcal{R} \equiv |E_+/E_-|$ where E_- (resp. E_+) is the decelerating (resp. accelerating) axial electric field within (resp. behind) the electron bunch; see Fig. 20 (b). The achieved \mathcal{R} and E_+ values as the structure geometry is varied are shown in Fig. 21. As $a \in [20, 300] \mu\text{m}$ and $b \in a + [20, 300] \mu\text{m}$ are varied the wavelengths of the excited wakefield modes change. The simulations show that profiles (b) and (c) of Fig. 19 can yield values of $\mathcal{R} > 2$. A possible configuration with $(a, b) = (20, 60) \mu\text{m}$, results in $\mathcal{R} \simeq 5.8$ with $E^+ \simeq 0.75 \text{ GV/m}$; see corresponding wake in Fig. 20 (b). Such high-field with transformer ratio significantly higher than 2 and driven by bunches produced in a superconducting linac could pave the way toward compact high-repetition-rate short-wavelength FELs .

Finally, the proposed technique could be adapted to non-ultrarelativistic energies using a two- (or multi-) frequency version of the velocity-bunching scheme . Such an implementation would circumvent the use of a BC and would therefore be immune to CSR effects.

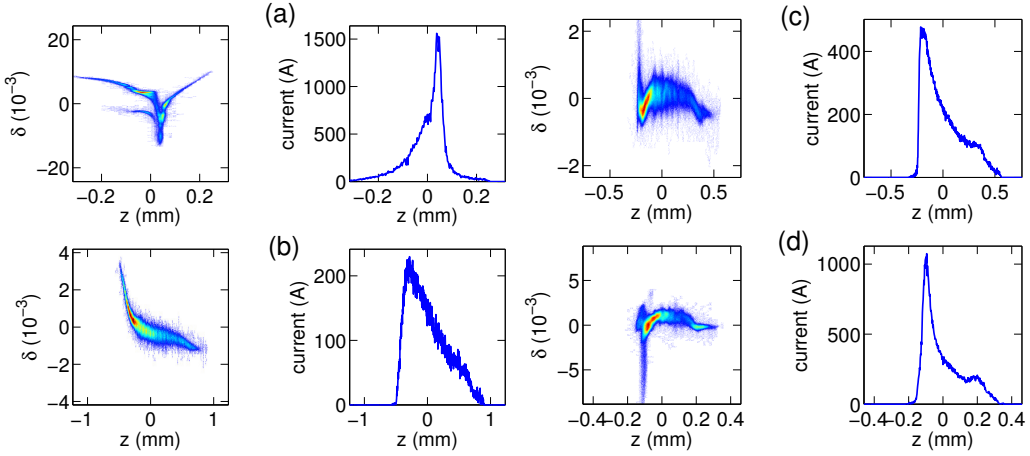


Figure 19: Snapshots of the measured longitudinal phase spaces (left column) and associated current profiles (right column) for different settings of the ACC1 and ACC39 accelerating modules. The values $(V_1, \varphi_1; V_3, \varphi_3)$ [in (MV, °; MV, °)] are: (150.5, 6.1; 20.7, 3.8), (156.7, 3.8; 20.8, 168.2), (155.6, 3.6; 20.6, 166.7), and (156.8, 4.3; 20.7, 167.7) for respectively case (a), (b), (c), and (d).

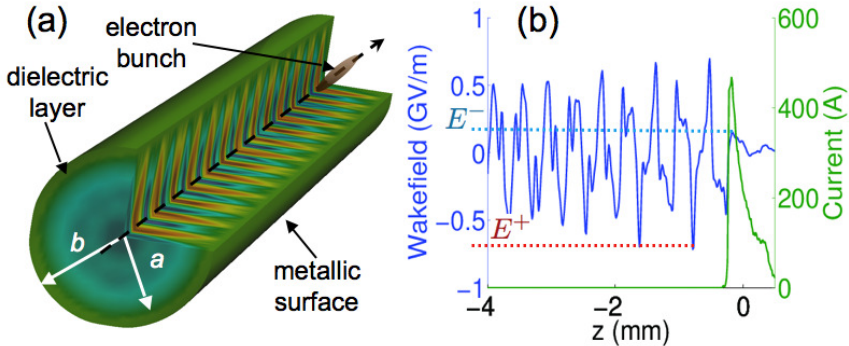


Figure 20: Cylindrical-symmetric dielectric-loaded waveguide considered (a) and axial wakefield produced by the current profile shown in Fig. 19 (c) for $(a, b) = (20, 60)$ μm .

4 EXPERIMENTAL SETUP FOR SLAB-DIELECTRIC STRUCTURE TEST AT FERMILAB

4.1 EXPERIMENTAL SETUP

The beamline configuration for our DWFA experiment is diagrammed in Fig. 22. The beamline comprises a L-band RF gun followed by two SCRF accelerating cavities (CAV1 and 2). The RF gun is nested in a pair of solenoidal lenses that can be used to produce beam with large angular momentum. Such a beam can be decoupled by a set of three

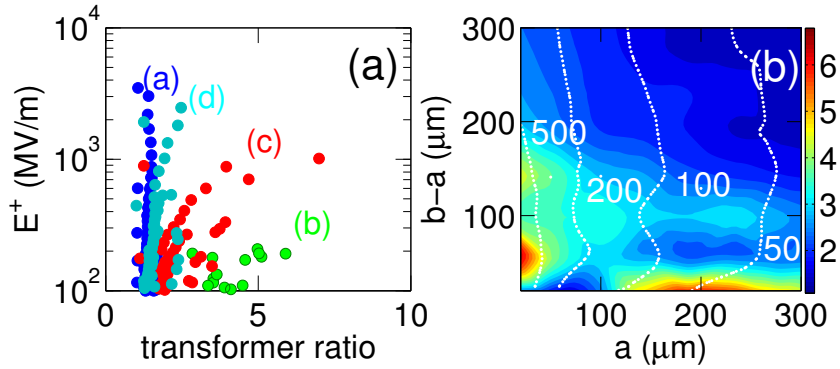


Figure 21: Simulated $\ddot{\Lambda}$ ratio versus peak accelerating field (a) for the four measured current profiles (displayed as different colors with label corresponding to cases shown in Fig. 19). Transformer ratio (false color map) as a function of the DLW inner radius a and dielectric layer thickness $b - a$ with corresponding $|E^+|$ shown as isolines with values quoted in MV/m for case (c) of Fig. 19.

skew quadrupole magnets downstream of CAV2 to produce flat beams – beams with high transverse emittance ratio – that can then be compressed using a magnetic chicane (BC1). The skew quadrupole magnets insertion is referred to as round-to-flat-beam transformer (RFBT). Downstream of BC1, a triplet is used to focus the beam inside the DLW structure mounted in a 2-axis goniometer; additionally, a linear stages will give control over the aperture of the DLW by varying the gap between the two slabs. The beam is finally drifted

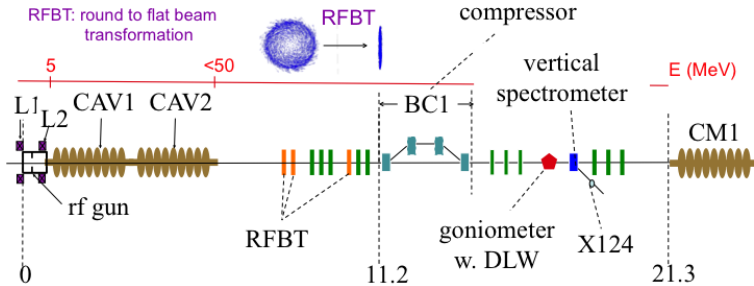


Figure 22: Layout of the ASTA photoinjector. L1 and L2 are solenoids, and CAV1 and 2 SCRF cavities. The green and red rectangles respectively represent normal and skewed quadrupole magnets. X124 is Ce:YAG a screen located in the dispersive section.

to the vertical spectrometer and directed to a Ce:YAG screen (X124) with full vertical size of 38 mm and located at a dispersion of $\eta_y = 0.44$ m permitting the measurement of beam spectrum of $\delta p/p \sim 9\%$ relative momentum spread. The high-resolution CCD (Prosilica GC 2450) could in principle enable resolution below $\delta p/p \sim 10^{-4}$ for an ideal zero-emittance beam. The zero-charge betatron functions at X124 viewer are shown in Fig. 23 as a function of betatron functions obtained at the waist ($\alpha_x = \alpha_y = 0$) in the DLW structure. The

focusing between the DLW structure and X124 screen is solely achieved by the dipole (no quadrupole magnets are presently installed in this section). For a vertical beta function

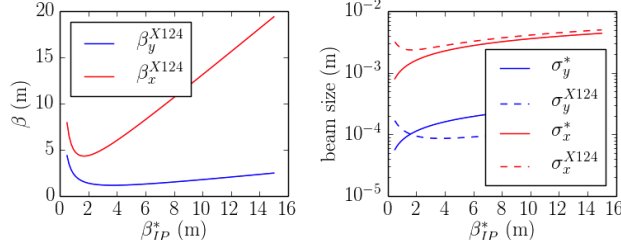


Figure 23: The zero-charge betatron functions (left) and the transverse RMS beam sizes (right) along the ASTA accelerator with flat beams.

of $\beta^* \simeq 2$ m at the center of the DLW, the resulting β function at X124 is $\beta_y^{X124} \simeq 1$ m limiting the energy resolution of the spectrometer to 1.8×10^{-4} (for a geometric emittance of ~ 6.3 nm (corresponding to 0.5 μm normalized with a Lorentz factor $\gamma \simeq 80$).

Finally, a diagnostics station located downstream of the vertical spectrometer will enable the detection and autocorrelation of THz radiation generated by the bunch passing through the DLW structure. The autocorrelation is performed with a Michelson interferometer employing a He-cooled InSb bolometer; see details in Ref. .

Our experiment relies on the production of a flat beam, i.e., a beam with large transverse emittance ratio . In our setup we produce flat beams with a low vertical emittance to mitigate horizontal-emittance-dilution effects arising in BC1 via space charge and coherent synchrotron radiation. Another benefit of this configuration is the low betatron contribution to the beam size at X124 given a vertical normalized emittance as low as $\varepsilon_y \simeq 0.3$ μm . An important challenge to overcome is the formation of compressed flat beam as described elsewhere .

4.2 START-TO-END SIMULATIONS

The start-to-end simulations detailed below were performed using particle-in-cell beam-dynamics program including ASTRA and IMPACT-T . The distribution downstream of the compressor was then matched to a waist at the DLW structure location with ELEGANT . To model the beam self-interaction with its wakefield in the DLW, we use a modified version of IMPACT-T described in Ref. . The dielectric-wakefield model is based on a 3-D Green's function approach and was successfully benchmarked against particle in cell finite-difference time-domain simulations . We consider a DLW structure composed of two parallel dielectric slabs. The separation between the inner surface and outer (metallized) surfaces is respectively $2a$ and $2b$. The dielectric thickness is $b - a$ and its relative permittivity is taken to be $\varepsilon_r = 5.7$ to correspond to diamond.

4.2.1 CASE OF SINGLE-MODE DLW STRUCTURES

Single-mode structures have the advantage to produce sinusoidal fields with known wavelengths. However since the beam's energy couples to a single mode, the resulting accelerating fields are generally smaller than the accelerating gradients achieved in multimode

structures.

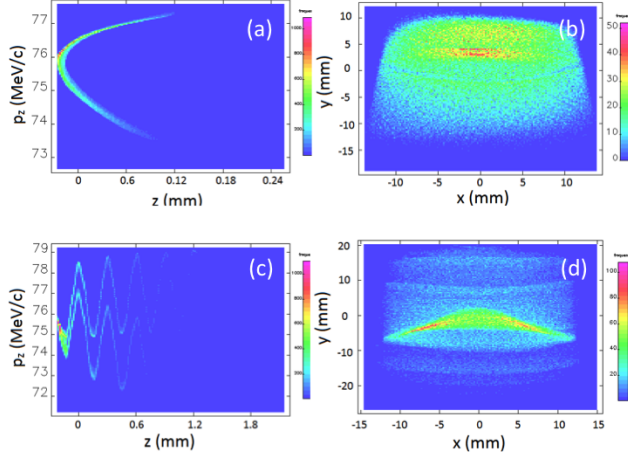


Figure 24: Longitudinal phase spaces (a,c) and associated transverse distributions at X124 (b,d) with (a,b) and without (c,d) a DLW structure. The DLW structure used for (c,d) has parameters $a=100 \mu\text{m}$, $b = 120 \mu\text{m}$, and $\varepsilon_r = 5.7$

Due to the limited measurement apparatus in the planned experiment, we must establish a method of decoding the information from the projected energy modulated beam onto X124. Figure 24(a,b) illustrates the nominal longitudinal phase space (LPS) and the associated transverse beam distribution at the X124 location when no DLW structure is inserted in the beam path.

A complication arising from the relatively long photocathode laser pulse (rms duration $\sigma_t \simeq 3 \text{ ps}$) regards the accumulation of a strong quadratic distortion on the LPS during acceleration in CAV1 and CAV2 which, after bunch compression results in a highly distorted distribution. The distribution has some benefits to the investigation of wakefields as the charge concentration in the bunch head lead to high peak current ($\sim 5 \text{ kA}$) that excites strong wakes while the long trailing electron population samples this wake over several periods. This feature is clearly demonstrated in Fig. 24(c) where the LPS immediately downstream of a DLW structure with parameters $a=100 \mu\text{m}$, $b = 120 \mu\text{m}$, and $\varepsilon_r = 5.7$ is shown. The resulting transverse distribution on X124 shows some horizontal bands that correspond to the local maxima of the observed energy modulations on the LPS. Because of the large number of modulations, some smearing occurs at X124. In addition, we note that the Cherenkov pattern resulting from the dependence of the accelerating field on the transverse coordinates can be clearly resolved at X124 and could provide insightful measurements for precise benchmarking of the 3-D model.

4.2.2 CASE OF MULTI-MODE DLW STRUCTURES

The high-peak current and narrow width of the bunch head is capable of exciting has a spectrum that extends close to 10 THz. It is therefore capable to excite higher-order modes possibly supported by the DLW structure. A simple way to enable multi-mode operation

of DLW structures consists of using of thicker dielectric thicknesses. Additionally, a larger thickness can also lead to higher accelerating fields in the DLW as multiple modes can constructively add up. The draw back being the lack of control on the superposition of the mode which can possibly lead to accelerating field region with smaller longitudinal extend compared to single-mode structures. Such a lack of control could lead to the acceleration of witness bunches with distorted LPS or would require very short witness bunches.

Figure. 25 shows examples of LPS and transverse beam distribution simulated at X124 for two dielectric structures with inner radius $a = 100 \mu\text{m}$ and outer radius $b = 150$ and $200 \mu\text{m}$. The experimental advantage for using multimode structures are the lower number of energy modulations which leads to fewer (and brighter) energy (horizontal) bands at X124.

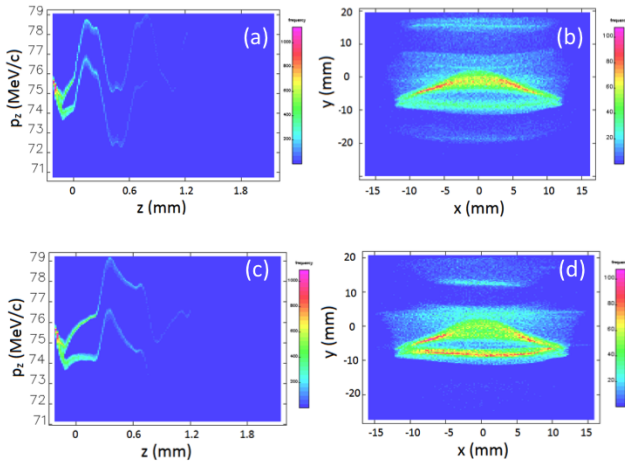


Figure 25: Longitudinal phase spaces (a,c) and associated transverse distributions at X124 (b,d) for a dielectric thickness of $\tau = 50$ (a,b) and $100 \mu\text{m}$ (c,d) DLW structure. The DLW structure other parameters are $a = 100 \mu\text{m}$, $b = a + \tau$, and $\varepsilon_r = 5.7$.

For the case of multimode structures the peak accelerating field are 110 and 120 MV/m for respectively a dielectric thickness of $\tau = 50$ [Fig. 25(a,b)] and $100 \mu\text{m}$ [Fig. 25(c,d)] while the single-mode structure was supporting a field amplitude of 105 MV/m [Fig. 24(c,d)]. We finally note that using a flatter beam could allow for smaller inner-aperture structure which could lead to larger accelerating fields. Another path to high axial field is the production of flat beams with higher peak current. This latter possibility would rely on the use of an enhanced compression scheme employing a high-harmonic accelerating cavity or wakefield linearizer to linearize the bunch's LPS prior to the BC1 chicane. Ultimately, given limited vertical aperture of the X124 screen (38 mm), the measurement of larger accelerating gradients would rely on the use of shorter DLW structures or lower-charge bunches.

4.3 CONCLUSION & OUTLOOK

We have demonstrated that ASTA could support tests of beam-driven acceleration based on a slab-symmetric DLW structure driven by flat beams leading to accelerating gradients larger than 100 MV/m.

We note that a possible extension will be the incorporation of longitudinally shaped bunches which could enhance the transformer ratio. Several techniques are currently under consideration ranging from transverse-to- longitudinal phase space exchanger , ad initio laser pulse shaping , and wakefield-induced shaper combined with ballistic compression . These different techniques, foreseen to be available at ASTA, range in their achieved precision of the control and in their complexity. These scheme will be throughly investigated at ASTA.

5 BENCH TEST OF A DIELECTRIC STRUCTURE

In slab DLW's the electromagnetic modes can be categorized into two types longitudinal section electric (LSE) and longitudinal section magnetic (LSM) corresponding respectively to the boundary conditions $E_y = 0$ and $H_y = 0$ at the vacuum-dielectric interface (the axis configuration is shown in Fig. 28. The lowest-order LSM mode is typically used for producing the axial electric field E_z necessary for acceleration. Fig. 27 presents the dispersion curve $k(\omega)$ associated to the LSM modes.

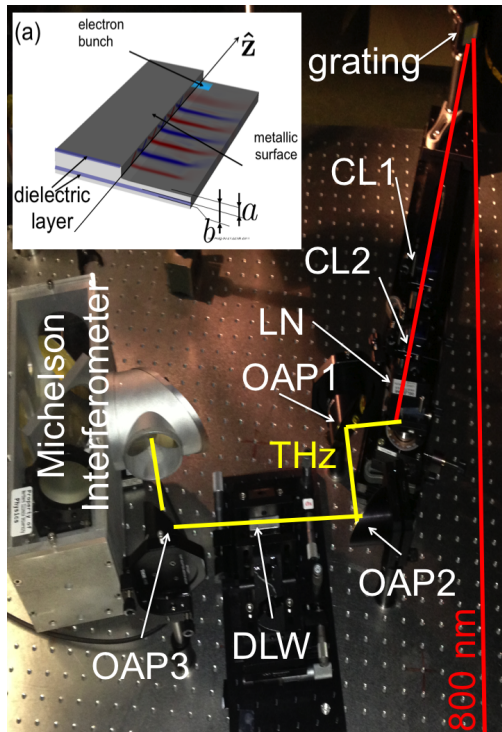


Figure 26: Experimental setup used to characterize DLW structures (photograph) and geometry of the DLW under consideration (inset schematic). The legend is as follows "CL", "OAP" and "LN" respectively stand for "cylindrical lens", "off-axis parabolic mirror", and "LiNbO₃ crystal". The red lines indicate the path of the 800-nm 4-mJ IR pulse and the yellow lines correspond to the THz beam.

In preparation for an experiment at the Advanced Superconducting Test Accelerator (ASTA) at Fermilab we are developing a THz bench test for slab DLWs. In this setup a THz pulse is used to probe the electromagnetic properties of the slab DLW using a near-field THz mapping technique similar to what was developed in Ref. . The method can be used to obtain spatial distributions of the modes along with their dispersion relations.

5.1 EXPERIMENTAL SETUP

The experimental setup to be used to characterize the DLW's is depicted in Fig. 26. The basic idea is to eventually perform a near-field mapping of a guided short THz pulse at the

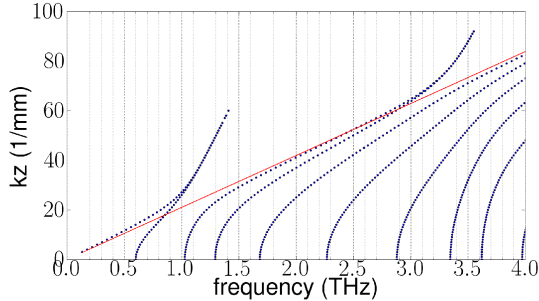


Figure 27: Dispersion relation associated to the LSM modes in a slab-symmetric DLW with parameter $a = 100 \mu\text{m}$ and $b = 120 \mu\text{m}$. The red line correspond to $k_z = 2\pi fc$.

input and the output of the DLW.

A 4-mJ, 800-nm amplified laser pulse produced by a commercial laser system is used to produce a THz pulse. The laser is obtained from regenerative amplification of a broadband $\delta\lambda \simeq 100 \text{ nm}$ pulse. Several method to produced THz were attempted: “conventional” optical rectification by impinging a ZnTe crystal with 100 cut and phase-matched optical rectification using a LiNbO₃ (LN) wedged crystal . Because of its significantly higher yield and relatively easy implementation we choose the latter method as shown in Fig. 26 and use a stoichiometric MgO(0.6%):LiNBO₃ crystal with a $5 \times 5 \text{ mm}^2$ entrance-face size.

The pulse impinges a 1200-lines/mm grating to provide the necessary wavefront tilt. A cylindrical lens focusing in the horizontal plane (CL1, $f = 15 \text{ cm}$) provides an approximate image of the grating onto the LN crystal. A second cylindrical lens (CL2) is used to focus the beam vertically. The typical spot on the LN crystal face is $w_x \times w_y \simeq 3 \times 0.5 \text{ mm}^2$. Upon exiting the LN crystal, the THz beam is collimated with an off-axis parabolic mirror (OAP1) and focused inside the DLW structure (OAP2). The transmitted THz beam is then collimated (using OAP3 and 4) and sent to a Michelson interferometer equipped with a Helium-cooled InSb bolometer. In a later stage we plan to have an electro-optical imaging diagnostics.

5.2 SIMULATION AND ANALYSIS OF A THZ PULSE PROPAGATION IN A SLAB DLW

To assess the performance of the described experimental setup we modeled the propagation of a THz pulse through the DLW and use these numerical results to develop analysis tools. The simulation of a THz pulse through the DLW were performed using the program VORPAL . VORPAL uses the conformal finite difference time domain (CFDTD) method to solve Maxwell’s equations. The geometry of the problem simulated with VORPAL appears in Fig. 28.

For the results presented below, a THz pulse is launched from the $(x = 0, y, z)$ plane using a time dependent current density

$$\vec{J}_z(t) = A_0 t \sin(\omega_1 t) \sin(\omega_2 t) \sin(\omega_3 t) e^{-(t-t_0)^2/(\tau^2)}, \quad (37)$$

where $\omega_i \equiv 2\pi f_i$ where $(f_1, f_2, f_3) = (0.8, 1.0, 1.2) \text{ THz}$, $t_0 = 2 \text{ ps}$, and the full-width

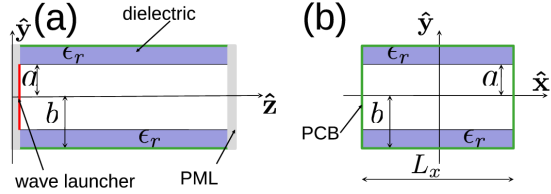


Figure 28: A diagram of the slab from the x-transverse direction (a) and the from the z-longitudinal direction (b). The slab is composed of a dielectric coating with dielectric permitivity ϵ_r surrounded by a perfectly conductive boundary (PCB). In the VORPAL simulation, we inject the THz pulse using a current \vec{J} to drive a short pulse in z. Lastly, to remove reflections and to artificially produce the pulse leaving the structure we implement a perfectly matched layer (PML). We record the signal on axis, near the PML.

half-max (FWHM) duration is $\tau = 1$ ps. Although the pulse peaks at frequencies f_i , its relatively large bandwidth $\delta f \simeq \tau^{-1} \simeq 1$ THz allows for the excitation of higher frequencies modes. The electromagnetic field of the guided pulse are recorded on a two-dimensional grid-line as a function of time at the entrance $E_u(x, y = 80 \mu\text{m}, z = 0, t)$ and at the exit $E_u(x, y = 80 \mu\text{m}, z = 2 \text{ cm}, t)$ (where $u \in [x, y, z]$ corresponds to the three field components).

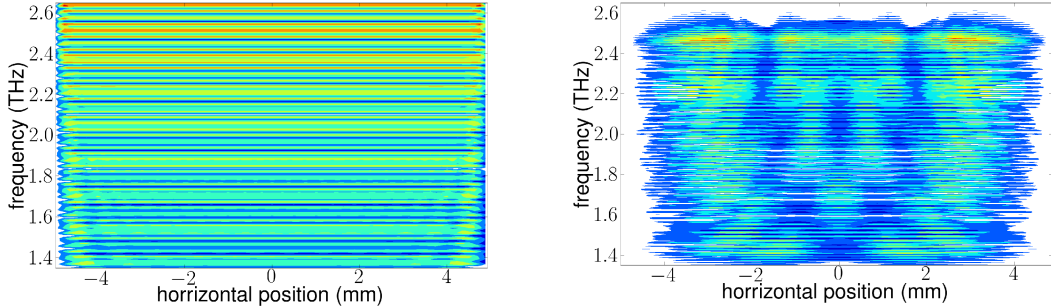


Figure 29: Fourier transform of the pulse at the entrance of the structure $|E_y(x = 0, y = 80 \mu\text{m}, z = 0, f)|$ (top) and a Fourier transform of the pulse at the end of the structure $|E_y(x = 0, y = 80 \mu\text{m}, z = 2 \text{ cm}, f)|$ (bottom).

The Fourier transform of the pulse before and after propagating through the structure provides a partial understanding of the propagation of the modes through the structure. The surviving frequencies correspond to the eigenmodes of the structure while components which have faded can be associated to the evanescent modes. Figure 29 shows the Fourier transform of the E_y component at the entrance and exit of the DLW structure. The spatial variations of the frequency content within the pulses is indicative of the mode's spatial distributions.

We import the signal recorded at the end of the structure into another program for spatio-temporal analysis. For each grid point recorded on the transverse line at the exit

of the structure, we use a moving window to scan through the signal temporally. At each window step, we perform a Fourier transform and record the strength of the Fourier component of a selected frequency. To reduce any unwanted artifacts, e.g., from sharp edges the moving windows is a Hann window

$$w(n) = 0.5 \left[1 - \cos \left(\frac{2\pi n}{N-1} \right) \right], \quad (38)$$

for an individual point n , of N sampled points.

In Fig. 30 we show the spatio-temporal distribution of the guided pulse associated to the filtered frequencies of 1.4 and 1.8 THz. Using this method, and comparing to the dispersion curve above, we can confirm the propagation of the LSM_{2m} and LSM_{3m} for the 1.4 THz component as well as the propagation of the LSM_{2m} , LSM_{3m} , and the near cutoff region of the LSM_{4m} which explains its tardiness passing through the structure. In addition to providing information on the modes' spatial distribution, the technique can also be used to deduce the group velocity of the modes.

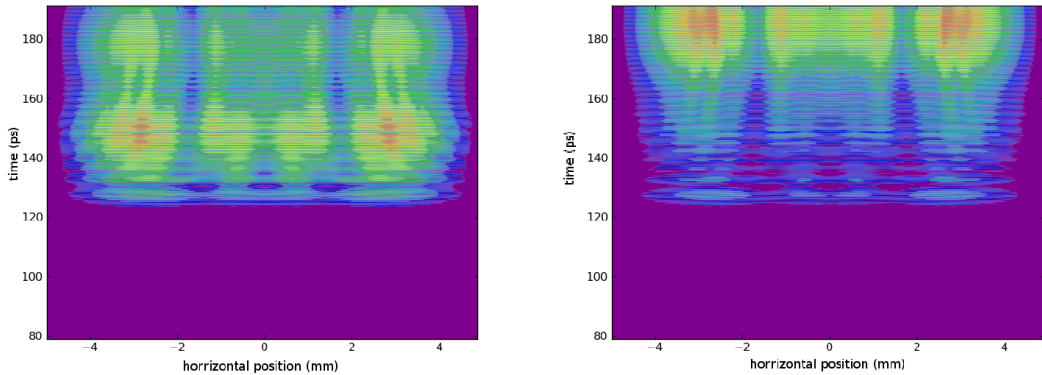


Figure 30: Spatio-temporal distribution of the guided pulse (shown in Fig. 29) filtered at 1.4 THz (top) and 1.6 THz (bottom).

5.3 STATUS AND CONCLUSION

An experimental setup to support the characterization of DLW structure was assembled and first results on the THz pulse production were recently measured. In this paper we presented numerical simulation to benchmark our analysis technique. Our results shows that quantitative information on the DLW mode can be obtained. The experiment is being carried used the laser available at the high brightness electron source laboratory (HBESL) at Fermilab National Accelerator Laboratory.

6 EDUCATION & COLLABORATION

One student, Mr. Francois Lemery, is currently being supported full time on this grant. Mr. Lemery joined this project in the Fall 2010 and has been working toward numerical modeling of dielectric wakefield accelerators. Mr. Lemery has been an active researcher and

presented his work at various international conferences. Most recently he gave two talks on electron-bunch shaping techniques and optimal current shapes for enhanced transformer ratio at the Advanced Accelerator Concept Workshop 2014. Mr. Lemery secured a one-year University dissertation-completion fellowship to finalize the work carried under the DTRA grant. He will graduate in Spring 2015.

In addition, another student not sponsored by this grant (but supervised by P. Piot) is partially involved on this project. Mr. Christopher Prokop, who joined the beam physics group in the summer 2008, obtained his Master in the summer 2009. Mr. Prokop's Master pertained to high-fidelity particle-in-cell simulations of table-top Terahertz coherent light sources based on the Smith-Purcell effect. Mr. Prokop extensively worked with the code VORPAL from Tech-X and brings his expertise by helping us setting up the problems to be simulated as part of this project.

This project was a joint venture with Tech-X and we have continuously collaborated with P. Stoltz, D. Smithe, B. Cowan, and J. Smith. We have especially been meeting regularly (in average monthly) to discuss our progress and problems. This collaboration has been extremely fruitful and led to several publications and contributing to our students training.

As part of this proposal we strengthen our relation with the German's national laboratory Deutsches Elektronen-Synchrotron (DESY) located in Hamburg, Germany. We had initially approached potential collaborator to perform a DWA experiment there. We were granted 36 hours of beam time on the Free-electron LASer in Hamburg (FLASH) facility in 2011. This is a commensurable contribution to our project (operating costs of the facility are \$ 5-10k/hour). We conducted an experiment to demonstrate we could shape the current profiles of electron bunches to enhance the performance of wakefield accelerators. This phase-I experiment resulted in very exciting results that was published in Physical Review Letters. Subsequently P. Piot visited DESY to discuss a possible DWA experiment at FLASH. The FLASH team was very receptive to such an experiment and offered significant support.

Finally, we collaborated with Euclid Lab. LLC and worked with personnel at this small-business innovative research company to specify and obtain dielectric-wakefield structures.

7 PUBLICATIONS, AND PRESENTATION

7.1 TALKS

1. F. Lemery, "Passive longitudinal-phase-space tailoring of non-ultrarelativistic beams with dielectric-lined waveguides", 16th Advanced Accelerator Concepts Workshop (AAC 2014), San Jose, CA, July 13-18, 2014 (working group 5).
2. F. Lemery, "Alternative Shapes and Shaping Techniques for Enhanced Transformer Ratios in Beam Driven Techniques", 16th Advanced Accelerator Concepts Workshop (AAC 2014), San Jose, CA, July 13-18, 2014 (working group 2).
3. F. Lemery, "Flat-beam-driven Dielectric-wakefield acceleration at ASTA", ASTA users' meeting, July 24, 2013, Fermilab. Batavia IL.

4. P. Stoltz, "Modeling of thermal effects in dielectric wakefield accelerators", APS March meeting, Baltimore MD (2013)
5. D. Mihalcea, "A dielectric-wakefield Energy doubler for the Fermilab's ASTA facility", High-brightness electron beam, Puerto Rico (HBEB13)
6. P. Piot, "Formation of Tailored Electron Bunches in Multi-Frequency Linacs", invited talk WG5, Advanced Accelerator Concept 2012.
7. P. Piot, "An Energy doubler DLW-based module for the ASTA facility at Fermilab", contributed talk WG4, Advanced Accelerator Concept 2012.
8. P. Stoltz, "Wakefield Generation in Compact Rectangular Dielectric Loaded Structures Using Flat Beams," 53rd Annual Meeting of the APS Division of Plasma Physics, Nov 14-18, 2011, Salt Lake City, UT.
9. P. Piot, "Generation of Electron Bunches with Tailored Current Profiles at FLASH", Bechleuniger Seminar, 08/01/2011, DESY-Hamburg, Germany.
10. P. Piot, "Electron bunch shaping for enhanced transformer ratio: ideas & issues", DWA-FEL workshop, 05/11/2011, Argonne IL.
11. D. Mihalcea, "High-gradient wakefield acceleration in dielectric-loaded structures", Accelerator Seminar, 05/05/2011, Fermilab, Batavia, IL

7.2 REFERRED PUBLICATIONS:

1. D. Mihalcea et al., "Three-dimensional Analysis of Wakefield generated by Flat Beams in Planar Dielectric Loaded Structures", Phys. Rev. ST Accel. & Beams 15 081304 (2012).
2. P. Piot et al. "Generation and Characterization of Electron Bunches with Ramped Current Profiles in a Dual-Frequency Superconducting Linear Accelerator", Phys. Rev. Lett. 108, 034801 (2012).
3. F. Lemery, and P. Piot, "Ballistic Bunching of Photo-Injected Electron Bunches with Dielectric-Lined Waveguides", accepted Phys. Rev. ST Accel. & Beams (2014).
4. P. Stoltz, et al., "Coupled thermo-electromagnetic simulations of beam-driven dielectric accelerator", in preparation

7.3 CONFERENCE PROCEEDINGS PAPERS:

1. F. Lemery, and P. Piot, "Passive longitudinal-phase-space tailoring of non-ultrarelativistic beams with dielectric-lined waveguides", Proceedings of the 16th Advanced Accelerator Concepts Workshop (AAC 2014), San Jose, CA, July 13-18, 2014 (in press).
2. F. Lemery and P. Piot, "Alternative Shapes and Shaping Techniques for Enhanced Transformer Ratios in Beam Driven Techniques", Proceedings of the 16th Advanced Accelerator Concepts Workshop (AAC 2014), San Jose, CA, July 13-18, 2014 (in press).

3. F. Lemery, D. Mihalcea, P. Piot, J. Zhu, "Planned High-gradient Flat-beam-driven Dielectric Wakefield Experiments at the Fermilab's Advanced Superconducting Test Accelerator", Proceedings of the 2014 International Accelerator Conference (IPAC14), Dresden, Germany, June 15 - 20, 2014 (in press).
4. F. Lemery, and P. Piot, "Temporal Electron-bunch Shaping from a Photoinjector for Advanced Accelerator Applications", Proceedings of the 2014 International Accelerator Conference (IPAC14), Dresden, Germany, June 15 - 20, 2014 (in press).
5. F. Lemery et al., "Toward a dielectric-wakefield energy doubler for Fermilab's advanced superconducting test accelerator", Proc. IPAC13, in press (2013).
6. F. Lemery et al., "THz bench test of slab-symmetric dielectric waveguide structures", Proc. IPAC13, in press (2013).
7. F. Lemery et al., "Performances of VORPAL-GPU for slab DLW structure", Proc. IPAC13, in press (2013).
8. P. Piot, et al., "Formation of Tailored Electron Bunches in Multi-Frequency Linacs", Proc. Advanced Accelerator Concept workshop (AAC12), in press (2012).
9. F. Lemery, et al., "Optimization of Drive-Bunch Profile for Enhanced Transformer Ration in Beam-Driven Acceleration Techniques", Proc. of the 2012 International Particle Accelerator Conference (IPAC12), 3012 (2012).
10. F. Lemery, et al., "Progress toward a high-transformer-ratio dielectric-wakefield experiment at FLASH", Proc. of the 2012 International Particle Accelerator Conference (IPAC12), 2167 (2012).
11. D. Mihalcea et al. "Wakefield Generation in Compact Rectangular Dielectric-Loaded Structures Using Flat Beams", Proc. of the 2011 Particle Accelerator Conference (PAC11), 340 (2011).
12. F. Lemery et al. "Experimental plans to explore dielectric wakefield acceleration in the THz regime ", Proc. of the 2011 International Particle Accelerator Conference (IPAC11), 2781, (2011).
13. P. Piot, et al., "Generation and Characterization of Electron Bunches with Ramped Current Profiles

DISTRIBUTION LIST
DTRA-TR-15-36

DEPARTMENT OF DEFENSE

DEFENSE THREAT REDUCTION
AGENCY
8725 JOHN J. KINGMAN ROAD
STOP 6201
FORT BELVOIR, VA 22060
ATTN: D. PETERSEN

DEFENSE TECHNICAL
INFORMATION CENTER
8725 JOHN J. KINGMAN ROAD,
SUITE 0944
FT. BELVOIR, VA 22060-6201
ATTN: DTIC/OCA

**DEPARTMENT OF DEFENSE
CONTRACTORS**

QUANTERION SOLUTIONS, INC.
1680 TEXAS STREET, SE
KIRTLAND AFB, NM 87117-5669
ATTN: DTRIAC